OULUN YLIOPISTO
UNIVERSITY of OULU

DEGREE PROGRAMME IN ELECTRICAL ENGINEERING

MASTER'S THESIS

HARDWARE IMPROVEMENTS FOR DETECTING MODULATED NEAR-INFRARED LIGHT IN DIFFUSE OPTICAL MEASUREMENTS OF THE HUMAN BRAIN

Thesis author	Leandro Marco Pérez.
Thesis supervisors	Matti Kinnunen, Teemu Myllylä.

Marco Pérez L. (2014) Hardware improvements for detecting modulated near-infrared light in diffuse optical measurements of the human brain. University of Oulu, Department of Electrical Engineering, Degree Programme in Electrical Engineering. Master's Thesis, 68 p.

ABSTRACT

Functional near-infrared spectroscopy (fNIRS) is a non-invasive *in vivo* brain imaging method. fNIRS systems can be used to detect diseases that alter the hemodynamics of the brain, but they are also applicable to the study of hemodynamics in healthy brains to investigate, for example, how brain hemodynamics change in response to external stimuli. The work carried out in this thesis involved improving parts of the light detection hardware that forms the core of a frequency-domain/spatially-resolved fNIRS system.

Different narrow band-pass filter configurations were analyzed to determine the best option for a system of that type. Among the various alternatives, multifeedback filters and resonator filters were simulated and compared. Finally, two different resonator filter sets were physically implemented using printed circuit technology.

The second part of the thesis describes the manufacture of six low-noise, high-sensitivity NIR light detectors designed to extend the light detection capabilities of the system. All these detectors were implemented on printed circuit boards.

After implementation, the circuits were tested separately and in combination with other parts of the system, achieving good results in both cases. The most significant result was the detection of blood flow pulsations from the finger and forehead of a subject using the designed light detectors in combination with the designed filters and a lock-in amplifier. This result shows that the circuits are fully functional and can be used to expand the capabilities of the fNIRS device.

Key words: near infrared, pass band filters, fNIRS, light detectors, human brain hemodynamics.

Marco Pérez L. (2014) Laitteistoparannuksia moduloidun lähi-infrapunavalon detektoimiseksi ihmisaivojen diffuusi optisessa mittausmenetelmässä. Oulun yliopisto, sähkötekniikan osasto, sähkötekniikan koulutusohjelma. Diplomityö, 68 s.

TIIVISTELMÄ

Toiminnallisella lähi-infrapunaspektroskopialla tarkoitetaan usein ei-invasiivista aivojen optista kuvantamista. Menetelmää voidaan hyödyntää aivoperäisten sairauksien tutkimisessa, mutta myös terveiden aivojen toimintojen tutkimisessa, esimerkiksi tutkimalla kuinka ulkoinen ärsyke aiheuttaa aktivaation aivoissa, näkyen menetelmällä mitattavissa olevina aivojen happitasojen muutoksina. Tämän diplomityön aiheena oli olemassa olevan laitteiston vastaanotintekniikan kehittäminen, jota käytetään lähi-infrapunavalon taajuusmodulointiin perustuvassa tekniikassa.

Useanlaisia kapeakaistaisia suodatinkonfiguraatioita analysoitiin parhaan suodatintyypin valitsemiseksi. Eri vaihtoehdoista valittiin ns. multifeedback- ja resonaattorisuodattimet, joita simuloitiin ja verrattiin keskenään. Lopuksi suunniteltiin kaksi resonaattorisuodatinsarjaa toteuttaen piirilevyllä. Diplomityön toisena osana suunniteltiin kuusi pienikohinaista ja herkkää lähi-infrapunavalovastaanotinta käytettäväksi olemassa olevassa laitteistossa. Kaikki vastaanottimet rakennettiin piirilevylle.

Suunnitellut piirilevyt testattiin erikseen ja yhdistettynä laitekokonaisuuteen, saaden siinä hyviä tuloksia sekä suodattimilla että vastaanottimilla. Testeissä veren virtauksen pulsaatioita pystyttiin mittaamaan sormesta ja aivoista otsalohkon alueelta hyödyntäen olemassa olevaa ns. lock-in tekniikkaa. Testitulokset osoittivat, että suunnitellut piirilevyt toimivat hyvin ja paransivat mittalaitteen vastaanottimen suoritustasoa.

Avainsanat: lähi-infrapuna, kanavanpäästösuodatin, fNIRS, valovastaanotin, ihmisaivojen hemodynamiikka.

TABLE OF CONTENTS

FOREWORD

I would like to thank the personnel of the Optoelectronics and Measurement Techniques Laboratory of the University of Oulu for welcoming me and giving me the opportunity to work with them and letting me use their resources to write this thesis.

Particularly warm thanks go to Teemu Myllylä and Matti Kinnunen, my thesis advisors, for their kindness and for all the things they have taught me. Additional thanks to Teemu for showing me around and explaining me about different aspects of the culture and traditions of Finland and, of course, for taking me to the airport.

Special thanks to my friend and member of the research group, Lukasz Surazynski, for advice about circuit design and soldering of electronic components and for the great time we had working together. I also wish to thank my friend and member of the research group, Aleksandra Zienkiewicz, for her company and for making every day fun to come to work.

Last but not least, I want to extend heartfelt thanks to my family for supporting me every day of my life, especially this year that I spent away from home.

LIST OF ABBREVIATIONS AND SYMBOLS

ADC	analog to digital converters
ASIC	application specific integrated circuit
BOLD	blood oxygenation level dependent
CBF	cerebral blood flow
CBV	cerebral blood volume
CW	continuous wave
DAC	digital to analog converter
DPF	differential path-length factor
EEG	electroencephalogram
FD	frequency domain
fNIRS	functional near-infrared spectroscopy
fMRI	functional magnetic resonance imaging
FPGA	field programmable gate array
ICG	indocyanine green
IR	infrared light
LED	light emitting diode
mBLL	modified Beer-Lambert Law
MFB	multifeedback
MRI	magnetic resonance imaging
NEP	noise equivalent power
NIBP	noninvasive blood pressure
NIR	near-infrared
NIRS	near-infrared spectroscopy
PCB	printed circuit board
PPG	photoplethysmogram
SNR	signal to noise ratio
SRS	spatially resolved spectroscopy
TR	time resolved

α	drift factor
A	attenuation
A_m	gain at the central frequency
A/W	amperes per watt
B	bandwidth
c	light velocity
C	capacitor
Cf	feedback capacitor
c_i	concentration of chromophore i
cm	centimeter
dB	decibels
E	energy
ϵ_i	specific absorption coefficient of chromophore i

e_n	amplifier voltage noise
F	Farad
f	frequency
fc	corner frequency
f_m	central frequency
G	gain in dB
g	gain in linear
h	Planck's constant
I_{sn}	shot noise
I_{jn}	junction noise
I_d	dark current noise
I_n	amplifier current noise
$I_{n,e}$	amplifier voltage noise
I_p	photocurrent
Hb	deoxyhemoglobin
$HbO2$	oxyhemoglobin
Hz	Hertz
J	Joule
K	Kelvin or Boltzmann's constant
kHz	kilohertz
m	meter
MHz	megahertz
mm	millimeter
nF	nanofarad
nm	nanometer
Q	quality factor
rad	radians
Rf	feedback resistor
R_{sh}	shunt resistor
s	jw
sec	seconds
U_{out}	output voltage
V	Volt
ω	angular frequency
w_m	angular frequency at f_m
λ	wavelength
Ω	Ohm

1. INTRODUCTION

Near-infrared spectroscopy (NIRS) is a hot topic of investigation, due to its application range. It is used in such diverse fields as the food industry, chemical and biochemical industry, pharmaceutical industry, agriculture and environmental monitoring, not to mention the medical sector, where its applications include diagnostics, healthcare and health monitoring. [1, 2]

Owing to the physical properties of NIR light and the non-destructive, non-invasive nature of the used methods, NIRS is highly suitable for continuous quality control of production lines, prepared food and raw materials, as well as maturation and irrigation control of agricultural crops, health monitoring of vegetation, soil and air analysis, and more [1, 2]. Especially interesting are applications in the field of medicine. The development of NIRS technology permits different parameters of the human body to be measured continuously *in vivo*. This would not be possible otherwise. In addition, NIR technology is cheaper and more portable and comfortable than other methods used for similar purposes, including magnetic resonance imaging (MRI) or positron emission tomography (PET) [3]. Among the most common medical applications based on using NIR light are non-invasive measurements of blood oxygenation and brain hemodynamics. In the near future, NIRS-related measurements may become a powerful tool for detecting several diseases and for monitoring health in situations where traditional methods are less reliable. It can be used to perform continuous measurements of critical patients or new-born infants, for instance. [3]

The central topic of this thesis is functional near-infrared spectroscopy (fNIRS), which involves the application of NIRS technology to measure brain hemodynamics. In medical applications, fNIRS is one of the most promising fields of development, due to the difficulty of conducting brain measurements with traditional methods. fNIRS technology has the potential to become the main tool for the investigation of the human brain, thanks to its capability to measure internal brain hemodynamics in real time in a simpler and cheaper way than traditional methods. Developing a non-invasive and continuous method to accurately measure brain hemodynamics is a main goal in this field of investigation and in the project of which this thesis forms a part. [4]

This thesis focused on the design and physical implementation of different circuits required by the light detection and signal processing hardware of an fNIRS device developed in the Optoelectronic and Measurements Techniques Laboratory at the University of Oulu. More specifically, the thesis sought to design and construct different sets of narrow bandpass filters used to filter detected signals after conversion from light to electricity. These filters are intended to replace the current ones, expanding their filtering capability and improving the system's signal-to-noise ratio (SNR). They also allow better separation of the different modulation frequencies used in the system, increasing its sensitivity and enabling the measurement of several channels at the same time. The second part of the thesis centered on improving the sensitivity of the detectors. This involved manufacturing six low-noise high-sensitivity NIR light detectors to be used in combination with the new filters.

1.1. Outline of the thesis

During the work conducted in this thesis, the following working methodology was adopted. First, a broad discussion about the needs of the project was held with the members of the research group. Having gathered that information, a small-scale study was conducted on the options available, the results of which were presented to the research team. One option was then selected, design work was carried out and simulations were run when appropriate. Finally, the chosen circuit was fabricated and tested. If any problems arose, additional modifications were made and new testing was performed until the desired results were achieved.

In the next sections, a detailed explanation of this work will be presented. Section 2 offers a detailed description of fNIRS and the main physical principles underlying it, including an outline of its origins and of the actual technologies used, as well as a discussion of the main problems to be solved when interpreting the results. In Section 3, a brief description of the actual fNIRS device will be given, while Section 4 provides a summary of the process of creating the filters, including the necessary theoretical background. Section 5 offers a brief introduction to light detectors and the process of constructing them. Next, the Conclusions section summarizes the work done and analyzes the results obtained. Finally, the thesis finishes up with a discussion of future lines of investigation and further development of the system. Each topic is introduced with a general description and a basic theoretical foundation for understanding the rest of the section. The final part of each section presents the results achieved.

2. FUNCTIONAL NEAR-INFRARED SPECTROSCOPY

Near-infrared (NIR) energy, also known as NIR light, is invisible electromagnetic radiation. Although no official concordance exists, some international organizations, such as the International Commission on Illumination, defines NIR light as electromagnetic radiation with wavelengths between 700nm and 1400nm. [5]

Infrared light (IR) was discovered by William Herschel in the 19th century. It was in 1800, when Herschel was working with sun filters that he realized that there was an invisible energy producing heat. Intrigued by this fact, he took a glass prism to divide sunlight into its different components and, using a thermometer, he proved that some kind of invisible radiation beyond red light heated the thermometer. This energy was called infrared. [6]

In 1881, after the invention of the photographic plate, which has some NIR sensitivity, Abney and Festing were able to record the spectra of some organic liquids in the range of 1 to 1.2 μm, the first important measurement and interpretation in NIR spectrometry [2]. In 1905, W.W. Coblentz published a series of papers with hundreds of recorded spectra of compounds in the IR region from 1 to 15 μm. [2]

During the first half of the 20th century, several investigations extended the spectral database of compounds, and in the 1950s, the first applications in chemical analysis appeared [2]. In 1977, F. Jöbsis published some results on the transparency of brain tissue to NIR light and the possibility of using a trans-illumination technique for continuous non-invasive measurement of oxygen saturation in tissue [7]. Tran-illumination was quickly replaced by reflectance mode-based techniques, due to excessive light attenuation in adults. NIR systems evolved rapidly and by 1985 the first studies on cerebral oxygenation were conducted by M. Ferrari and expanded by others after him, ending with the development of functional near-infrared spectroscopy (fNIRS) [8, 9].

2.1. Measurement of hemodynamics using fNIRS

fNIRs is a non-invasive brain imaging method that measures the concentration of light-absorbing substances using near-infrared light, allowing us to record hemodynamics related to brain activity. Measurements with fNIRS are based on specific physiological and physical principles: cerebral blood flow (CFB) increases in active brain areas, hemoglobin molecules of blood absorb NIR light, the oxygenation level of hemoglobin changes its optical properties, tissue is relatively transparent to NIR light, and NIR light scatters strongly in all directions in tissue. [10]

The two principal chromophores of human blood are oxyhemoglobin (HbO2), i.e., blood hemoglobin combined with oxygen, and deoxyhemoglobin (Hb), which is oxyhemoglobin that has released its oxygen [11]. These two chromophores have different absorption ratios for NIR light, with Hb absorbing more than HbO2. By comparing the absorption spectra of the two chromophores, it is possible not only to measure the volume of blood in a region, but also the oxygenation level of this blood. Figure 1 shows the absorption spectra of the two chromophores [12, 14]. As seen, the absorption coefficient of the chromophores varies at different wavelengths. Also shown is the isosbestic point, which is a point in the NIR region, at around 810 nm, where the absorption coefficients actually coincide. To calculate relative hemoglobin

concentration, it is necessary to use two different wavelengths, one above this point and one below it. [13]

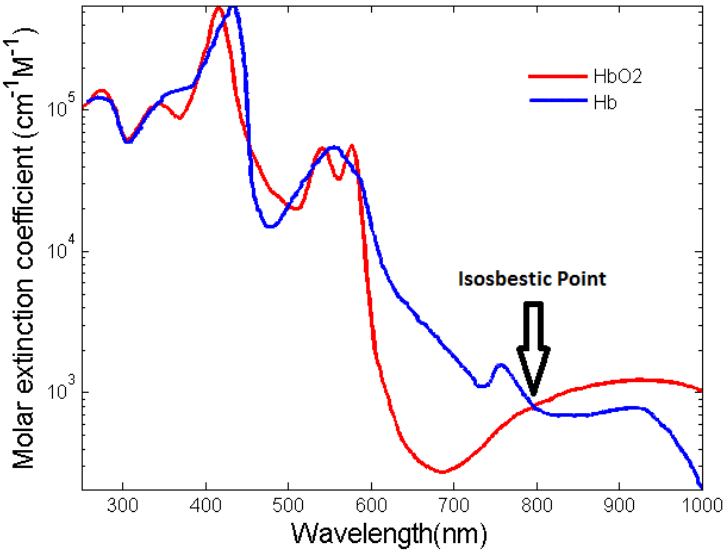

Figure 1. Absorption spectra for HbO2 and Hb, adapted from [12, 14].

The NIR range of the spectrum (650-950 nm) is especially suitable for these measurements, because of tissue transparency at these wavelengths, which allows deeper light penetration into the brain. Light is guided to the head through an optical fibre placed on the scalp. Having entered the head, NIR light scatters differently in different tissues, enabling measurements of intracranial structures, including the superficial layers of the brain. Scattering is a physical process whereby some forms of radiation, including light, sound and moving particles are deflected from their straight trajectories and forced to move in one or more different paths, due to non-uniformities in the medium they pass through [15]. Light scattering is caused by microscopic and macroscopic boundaries in tissue and interlayer discontinuities of intracranial structures caused by changes in the refraction index [10]. Although cells themselves form complex structures with different refraction indices that contribute to overall refraction, the most important scatterers are inside cells [15]. Subcellular organelles are comparable in size to the wavelength used, and therefore produce high anisotropic forward-directed scattering, which is the largest contributor to scattering in tissue [15]. As shown in Figure 2, the sensing volume of light scatters in a banana shape, entering the tissue from the fibre source contact point and returning to the surface at a different point. The longer the distance between the source and the detection point, the deeper the light travels. [16]

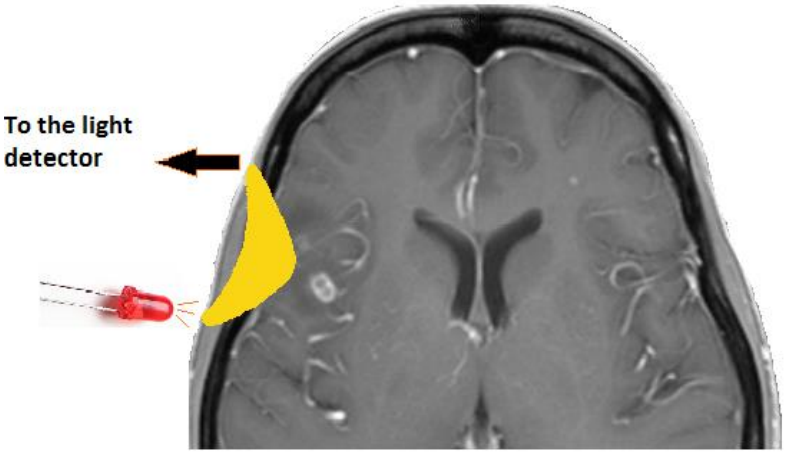

Figure 2. Photon travel path forms a banana shape from the illumination point to the detection point.

To summarize, fNIRS involves conducting light into the head and measuring back-scattered light to derive brain hemodynamics caused by brain activity, i.e., blood oxygenation and blood volume, through the measurement of the two principal chromophores of blood: HbO2 and Hb.

2.2. Modified Beer-Lambert Law

The concentration of HbO2 and Hb is related to light attenuation in the illuminated tissue. If the concentration is relatively small, it can be modelled with the modified Beer-Lambert Law (mBLL). [10]

$$A(t) = log\left(\frac{I_0}{I(t)}\right) = A^* + G + \sum_{i=HbO2,HbR} \epsilon_i \,.\, c_i(t) \,.\, d \,.\, B \quad , \quad (1)$$

where A is the attenuation, I the detected light intensity, I_0 the light intensity entering the tissue and A* time invariant attenuation caused by chromophores other than HbO2 and Hb. G is a time-invariant term representing unknown scattering losses, ϵi and ci are the specific absorption coefficient and the concentration of the chromophore i, d the geometrical distance between the illumination and detection point and B the differential path-length factor (DPF). [17, 18]

By using several wavelengths, the mBLL can be used to estimate changes in HbO2 and Hb, but in the absence of additional information, their absolute concentration cannot be measured, since scattering losses in tissue are unknown. Measuring the absolute concentration of the two chromophores requires using computerized Monte-Carlo simulations and physical models to estimate photon paths in tissue and to calculate scattering losses. [9, 10]

For the mBLL, it is assumed that the concentration of other chromophores is constant during the measurement, due to their slow rate of change relative to HbO2 and Hb. Another assumption is that the measured volume is homogeneous, which is not true of the human head, which, in addition to the brain, also contains various other tissue layers. Thus, the distance light travels in brain tissue is just a part of its

total travel distance. As a result, the estimated variation of HbO2 and Hb is smaller than in reality. Also the partial volume effect, i.e., changes in blood circulation in the scalp, distorts the results. [10]

Improving the results obtained with fNIRS involves fine-tuning the determination of light path length, enhancing the radiation power of light sources and detector sensitivity, and improving discrimination between signals recorded from the brain and those originating from the scalp and intermediate layers of the head. This can be achieved by assuming a specific shape for the hemodynamic response to brain activity and, in conjunction with multidistance recordings, adding heart rate and blood pressure measurements as explanatory variables to the model. [10]

2.3. FNIRs technologies

On the basis of their operation principle, commercial and experimental fNIRS devices fall into four broad categories: continuous-wave (CW), spatially-resolved (SR), time-resolved (TR) and frequency-domain (FD) spectroscopy. [9]

Being the simplest fNIRS technique, continuous-wave spectroscopy has the longest track record [10]. This technique employs light-emitting sources at a constant frequency and amplitude, measuring changes in light intensity and using the mBLL to derive changes in the relative concentration of hemoglobin. As light paths cannot be measured with CW, the absolute concentration of blood chromophores cannot be determined. However, this limitation can be circumvented by additional information from Monte-Carlo simulations and physical phantoms.

Spatially-resolved spectroscopy consists of using several detectors at different distances from the source to measure the relative ratio of chromophores for different photon path lengths. In this method, chromophore ratios are obtained from different tissue layers, from which their oxygenation levels can be calculated. To increase its characterization capability, SRS can be used in combination with the continuous-wave or frequency-domain method. Moreover, it allows minimizing the partial volume effect, resulting in more accurate measurements of brain tissue hemodynamics. [9, 10, 11, 19]

The time-resolved technique consists of sending very short light pulses, with a pulse length of the order of picoseconds, through the probed volume to measure the time it takes for the pulses to reach the detector. Of the four fNIRS techniques, it is the most complex and costly one but, by determining the delay times of the pulses, it enables us to distinguish signal components that have most probably reached brain tissue. With this method, we may calculate the absolute concentration of blood chromophores and the path length of light in various tissues. [9, 10, 11]

Frequency-domain (FD) spectroscopy involves modulating the intensity of light at radio frequencies and to measure the amplitude, phase and average intensity of the signal after it has passed through the tissues of interest. This technique is currently becoming the most widely used, due to a good balance between complexity and measurement quality. It allows calculating absorption coefficients without knowing the photon path length. Among its major advantages are sampling rate and accurate separation of absorption and scattering effects, which allows a more accurate determination of relative chromophore concentration rates, although additional data is needed to calculate absolute rates. Although the method does not permit the discrimination of deep and shallow components, it can be easily combined with the

spatially-resolved method to separate these components. This makes it one of the best options for fNIRS measurements. [19]

A schematic of the three main methods is presented in Figure 3. This graphical description illustrates the different emitting sources and the most important parameters considered when analyzing data collected with each method.

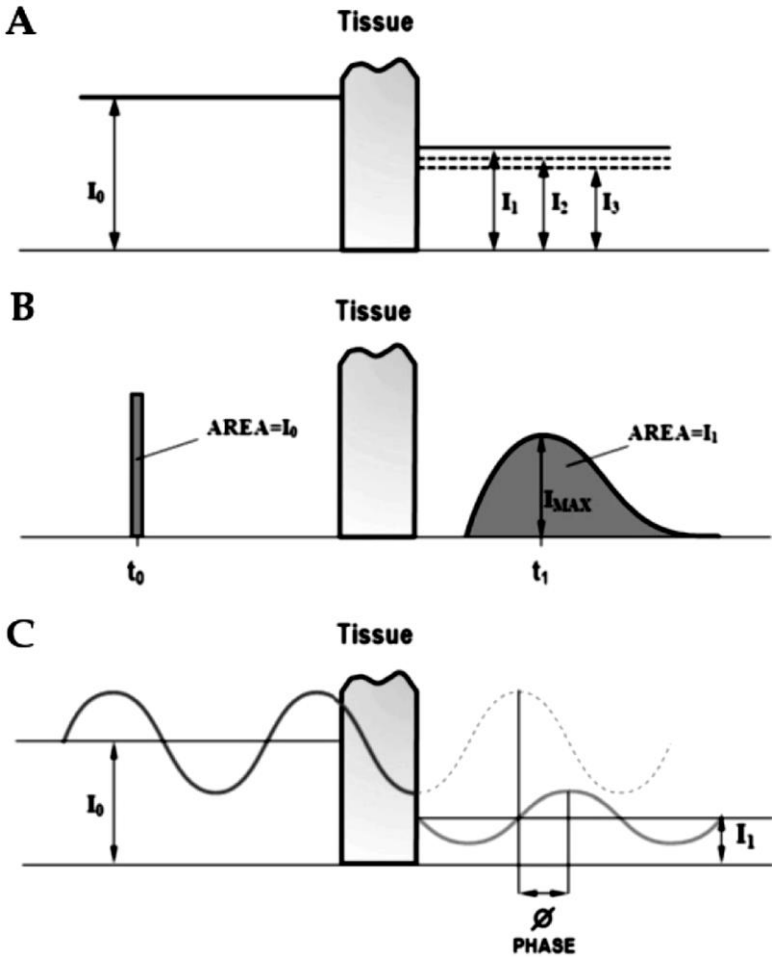

Figure 3. (a) Continuous-wave/spatially-resolved spectroscopy, (b) time-resolved spectroscopy, (c) frequency-resolved spectroscopy, adapted from [19].

2.4. FNIRS signal interpretation

fNIRS measurements are based on the attenuation of NIR light as it passes through brain tissue. However, this attenuation is influenced by several factors that must be taken into account to achieve realistic results for brain oxygenation and hemodynamics. [19]

2.4.1. Arterial/Venous ratio

The use of NIRS allows measuring oxygen saturation in small areas. Regional blood flow, however, consists of arterial, venous and capillary flows. Consequently, NIRs measures the mean cerebral tissue oxygenation level from the arterial, venous and capillary blood comprising the sampling volume. Normal hemoglobin distribution in the cerebral cortex is 70% for venous and 30% for arterial blood. Nonetheless, these ratios vary considerably between different people and can differ significantly from a person's actual tissue oxygen saturation level. [19]

In addition to oxygenation ratios, the attenuation of NIR light may also be affected by other parameters, including blood volume, blood pressure and blood flow, i.e., the velocity of blood. As these parameters are closely related, the absolute amount of blood chromophores may change, although the oxygenation level stays constant. This should be considered in the interpretation of measurement results, especially in critical care situations. [19]

One major problem with the fNIRS method is that the cerebral signal is not isolated, and multiple components coming from the outer layers of the head are mixed with the signal of interest. One solution to this problem is the use of multidistance detectors to separately detect cerebral signals and those originating from the external layers of the head. [10, 19, 20]

Separation of the transmitter and receiver is an important factor when detecting photons that travel deep into tissue, because mean penetration depth is approximately one third of the transmitter/receiver distance [21, 22]. Thus, a closely positioned detector can be used to record signals from the upper layers of the head, while a detector placed further apart from the transmitter detects deeper signals. The right distance for detecting signals in superficial tissue layers is 3 cm, while 3.5 cm or more is a good starting point for the detection of cerebral signals. Measuring outer signals separately and using signal processing allows distinguishing them from signals reaching brain tissue. [10, 19]

However, as regular fNIRS does not use this technique, it cannot differentiate between cerebral and extracerebral hemodynamics. Changes in external hemodynamics that occur during exercise may not be related to changes in cerebral hemodynamics.

3. DESCRIPTION OF THE FNIRS PROTOTYPE

The prototype fNIRs system, the target of this thesis, was developed and built in the Optoelectronic and Measurement Techniques Laboratory of the University of Oulu, Finland.

Combining frequency-resolved and spatially-resolved spectroscopy, the system uses a sinusoidal signal in the kHz range to modulate the amplitude of light emitted by the source and measures reflected light at different distances. This allows coherent detection of the signal with a high signal-to-noise ratio (SNR) using lock-in amplification. In addition, different light-emitting diodes (LEDs) can be modulated at different frequencies allowing the separation, processing and analysis of detected signals, thus encoding them. The motivation for using several detectors at different distances is that it allows measuring physical changes occurring in different layers of the head. After processing of all signals, brain hemodynamics can be separated from those taking place in the superficial layers of the head. [11, 23]

The system is composed of different functional blocks, including power-LED drivers, lock-in amplifiers, a programmable function generator, a data acquisition block and a microcontroller-based measurement control block [11]. Most of these blocks are software-based, as the software approach offers some advantages once the initial development stage has been completed. However, when the number of channels grows, so does the amount of resources required by data processing. The other main drawback of a software-based system is the limited frequency band at which common data acquisition cards can work. Mainly for these two reasons, it was decided to convert some of the software-based functional blocks to hardware-based technology.

In particular, the function generator block and lock-in amplification block were implemented in hardware. Lock-in amplifiers are locked to the frequencies used in light modulation, from 1 kHz to some tens of kHz. Due to the Nyquist principle, the data acquisition card must work at least at double the lock-in frequency; and the higher the frequency, the more expensive the data acquisition card required. When using hardware lock-in amplifiers, the frequency limitation, on the order of MHz, is marked by the chip of the lock-in demodulator. After lock-in demodulation, the frequencies present in the signals tend to be lower than 10 Hz, being the result of physical changes in the head. These low-frequency signals permit the use of cheap data acquisition cards. Figure 4 presents a block diagram of the system.

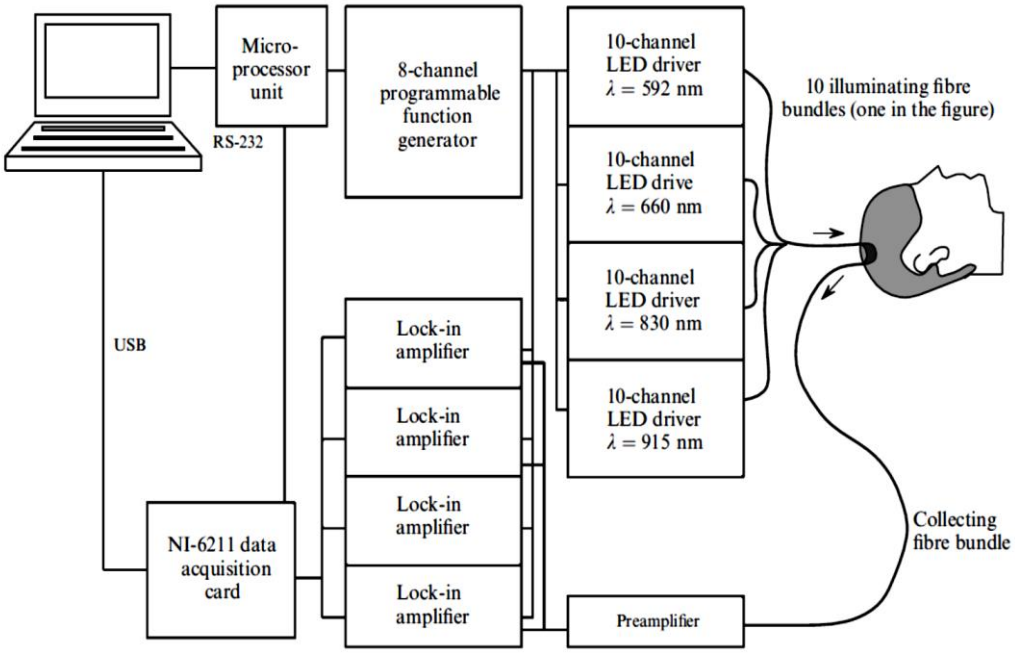

Figure 4. Block diagram of the fNIRs system. [11]

As seen, the system comprises multiple blocks, of which only the LED drivers and preamplifiers are now hardware-based. All remaining data processing and signal generation is realized by software, more specifically, by LabVIEW running on a regular laptop. In the next sections, a basic foundation will be provided for understanding the different aspects of the work presented in this thesis, together with a detailed description of the work.

4. NARROW BANDPASS FILTER DESIGN

An important contribution of this thesis to the improvement of the fNIRs system of the University of Oulu included developing filters used after the light detector. They are needed to separate the different channels used in the measurements, particularly the different wavelengths used to drive the LEDs, but they also play a role in improving the SNR of each channel and help to reduce cross-talk between channels at the input of the lock-in demodulator.

Due to the wavelengths selected to drive the LEDs and the low level of the detected signal, a high gain narrow passing band was needed with steep slopes in the transition bands. Two different sets of filters were designed, one with central frequencies of 1, 2, 3 and 4 kHz and the other with central frequencies of 6, 7, 8 and 9 kHz. The desired passing band was around 100 Hz with the maximum possible gain in the passing band, and 20 decibels (dB) of attenuation in the stop band. With these target characteristics in mind, different configurations where designed and simulated, and the selected one was physically implemented and tested.

4.1. Introduction to filter design

An electric filter is a quadrupole with the capacity to attenuate certain frequencies of the spectrum of the input signal, while allowing other frequencies to pass through. Filters can be classified on the basis of three main aspects: implementation technology, the function they perform and the mathematical function used to approximate the desired response curve.

4.1.1. Filter implementation technology

On the basis of the used technology, filters come in three different types: passive, active and digital filters.

Passive filters are built exclusively with such passive components as resistors, capacitors and coils, so they do not need a power supply. Though cheapest in price and easier to implement than the other types, they have some disadvantages. They exhibit attenuation in the passing band and since the slope in the transition band is not steep, the attenuation band must be separated sufficiently from the passing band. Moreover, due to their big size, coils are non-viable for low frequencies and capacitor values start growing exponentially.

Active filters use an operational amplifier as core technology. Constructed of active elements, they need a power supply to feed them. Active filters use mature technology with optimal characteristics for filter design, such as high input impedance, low output impedance and high gain for low to medium range frequencies. This was the technology we used in filter design, as it offers flexibility, stability, ease of implementation and relies on low-cost components.

Digital filters use analog to digital conversion of the analog signal. The resulting binary signal is then processed by software running on microprocessors, which perform the necessary mathematical operations on the input data and finally reconstruct the analog signal. This system employs such digital components as analog-to-digital converters (ADC), microprocessors, field-programmable gate arrays (FPGA), application-specific integrated circuits (ASIC) and digital-to-analog

converters (DAC). Being the most expensive technology, costs increase hugely with increasing converter sampling rate. On the other hand, when a great number of channels must be processed, digital filters can be a more affordable option than active filters. [24]

4.1.2. Filters according to their transfer function

The transfer function is a mathematical model that relates a filter's output response to its input through a coefficient. A graphic representation of the transfer function of a filter allows us to observe its behavior in relation to the used frequency. There are four main different transfer functions and, thus, four different filter configurations: low-pass filter, high-pass filter, bandpass filter and rejecting-band filter. [24]

Low-pass filters only have gain for frequencies below a specific corner frequency (f_c) and attenuate all frequencies above it. Calculated from the transfer function, f_c depends on the structure of the filter. The main design parameters for these configurations are the corner frequency of the passing band, maximum attenuation in the passing band, maximum ripple in the passing band, slope in the transition band, and minimum attenuation in the attenuated band. Figure 5 shows a graphic representation of the transfer function of a standard low-pass filter. [25, 26]

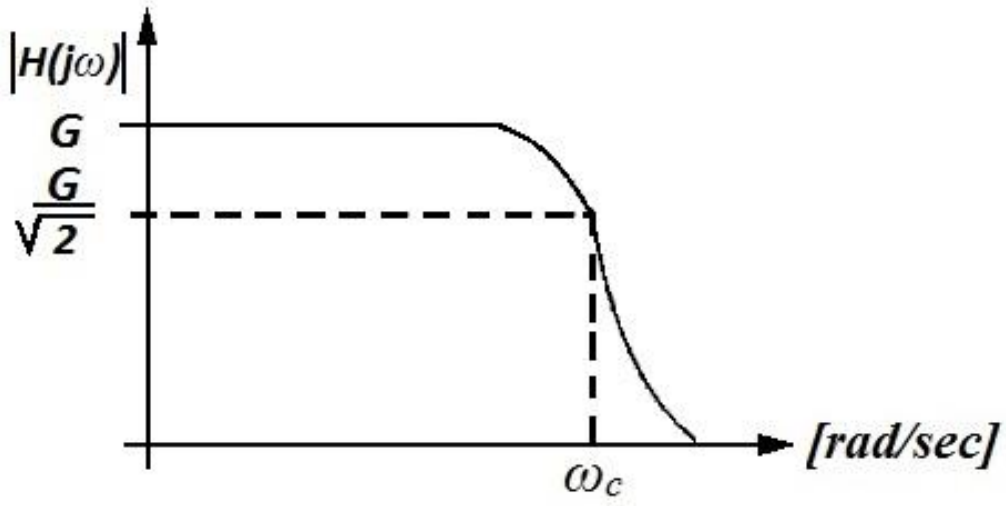

Figure 5. Moduli of the transfer function of a low-pass filter, where G is gain and ω_c is $2\pi fc$.

High-pass filters are complementary to low-pass ones. They add gain at frequencies above the corner frequency, while those below it are attenuated. Their design parameters are identical to those of low-pass filters. Figure 6 presents the corresponding transfer function.

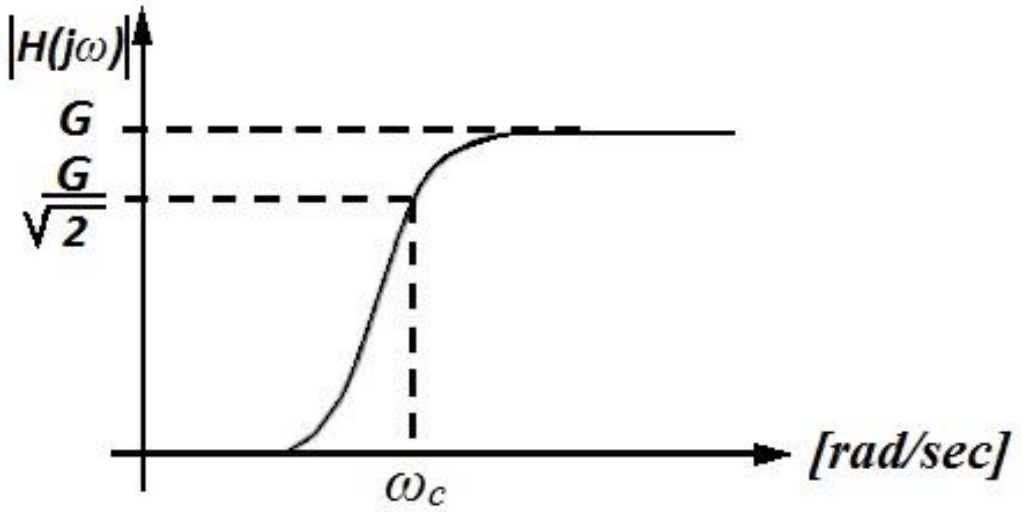

Figure 6. Moduli of the transfer function of a high-pass filter.

Bandpass filters only have gain in a limited range of frequencies. Central design parameters are the lower and upper corner frequency, central frequency and the quality factor Q that measures the selectivity of the filter, i.e., how narrow the passing band is in comparison with the central frequency. We will analyze this filter in detail in the following sections. Figure 7 shows the transfer function of this type of filter. [26]

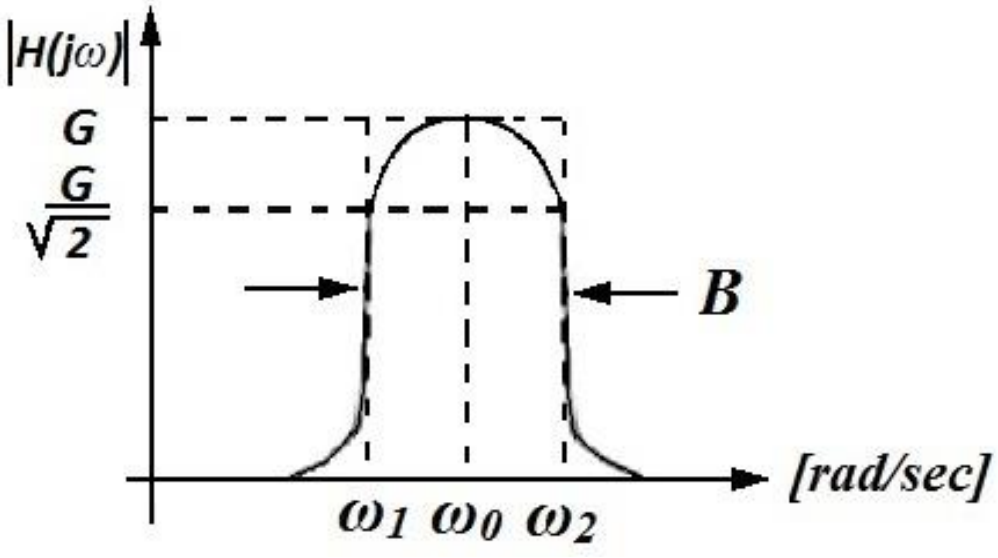

Figure 7. Moduli of the transfer function of a bandpass filter, where G is gain, ω_0 is $2\pi f_0$, B is bandwidth, and ω_1 and ω_2 stand for the lower and upper corner frequency, respectively.

Rejecting-band filters are complementary to bandpass filters. They attenuate all frequencies between the lower and upper corner frequencies, having gain for all other frequencies. They are useful, for example, when we want to remove an alternating current component that is spoiling our signal, such as the 50 Hz noise of the power line. Their design parameters are the same as those of bandpass filters. Figure 8 illustrates their transfer function.

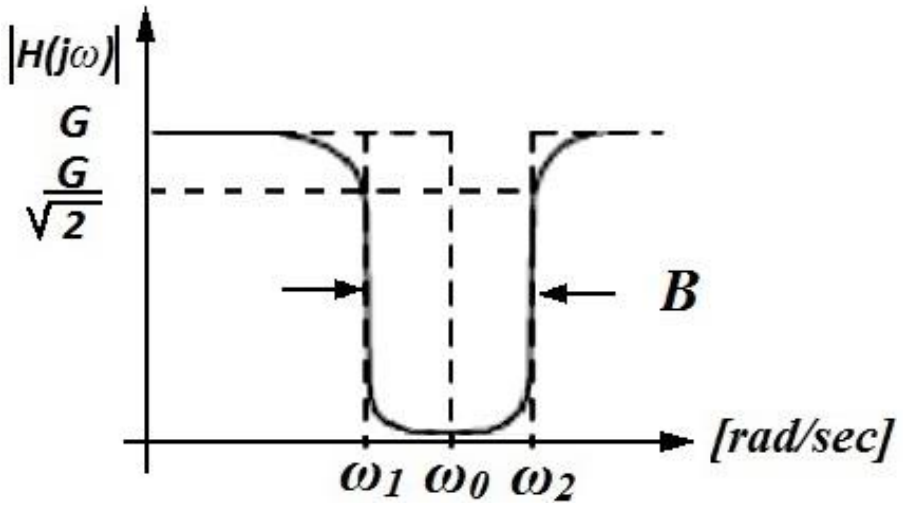

Figure 8. Moduli of the transfer function of a rejecting-band filter, where G is gain, ω_0 is central frequency, B is bandwidth, and ω_1 and ω_2 are the lower and upper corner frequency, respectively.

4.1.3. Mathematical functions in filter design

Filters can be classified by the mathematical function used to approximate the transfer function. There are four main mathematical functions used in filter design: Butterworth, Chebyshev, Bessel and Cauer (aka elliptic). They are complex mathematical models, and as they fall outside the scope of this thesis, we shall only discuss the main characteristics of the resulting filters.

Butterworth filters are basic filters designed to provide the flattest response in the passing band. After fc, their gain decreases 20.N dB per decade (N is the number of poles in the filter). [26]

Chebyshev filters have a high roll-off, i.e., a narrow transition band, but on the other hand, they have ripple in the passing or the non-passing band. In general, these filters have the closest transfer function to the ideal one. [26]

Bessel filters are designed to have a lineal phase in the passing band to avoid signal distortion and are, therefore, commonly used in audio applications. Then again, they have the disadvantage of a bigger transition band than the other filters.

Cauer, or elliptic, filters are the most complex to analyze and design. They have the narrowest transition band, but also ripple in both the passing and non-passing band. [26]

4.2. Noise study of the detected signal

The main reason for implementing a filter stage in a NIR device is to remove unwanted external or internal signals that are mixed with the signal of interest, degrading its quality and, in many cases, making detection impossible.

In the case of light receivers, the detection threshold is determined by the noise characteristics of the frontend. In light detectors, the main sources of noise are the photodiode and the amplifier. Total noise in the detector can be calculated as the square root of the sum of squares of the different noise sources,

$$I_n^{Tot} = \left(I_{sn}^2 + I_{jn}^2 + I_f^2 + I_n^2 + I_{n,e}^2\right)^{1/2}, \quad (2)$$

where I_{sn} is shot noise; I_{jn} is junction noise; I_d is dark current noise ; I_n is amplifier current noise and $I_{n,e}$ is amplifier voltage noise. [11]

Our NIR system employs a transimpedance op-amp to reduce noise. Figure 9 shows the equivalent circuit for this configuration. [11]

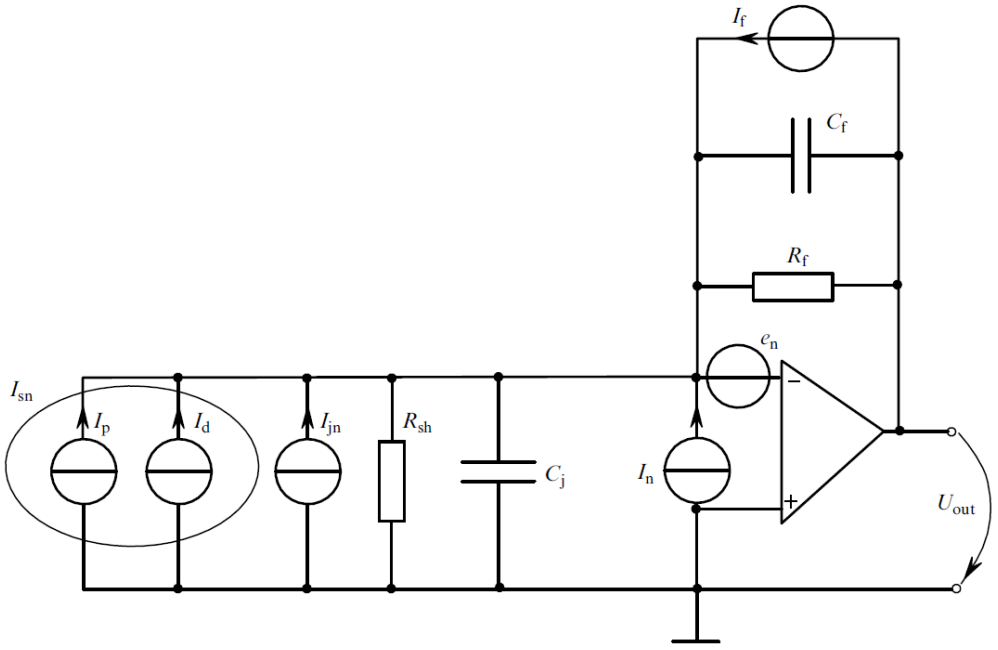

Figure 9. Equivalent circuit of the photodiode and amplifier with their noise sources, where R_f is the feedback resistor, $R_{sh}$is the shunt resistor, C_f is the feedback capacitor, C_j is the junction capacitor, I_d is the dark current, I_p is the photocurrent, e_n is the amplifier voltage noise and U_{out} is the output voltage. [11]

Greatest contributors to overall noise are the amplifier and the photodiode, while other noise sources are negligible. Careful selection of the feedback resistor of the amplifier permits the thermal noise factor to be reduced to the point that it can be ignored,

$$I_f = \left(\frac{4 \cdot k \cdot T \cdot B}{R_f}\right)^2 , \quad (3)$$

where $k = 1.381 \cdot 10^{23}\, J \cdot K^{-1}$, T is the temperature in Kelvins, B is the bandwidth in Hertz and R_f is the feedback resistor in Ohms. As shown in the equation, the noise value can be reduced using high resistance in the feedback loop [11]. This allows the total noise formula to be simplified as shown below,

$$I_n^{Tot} \approx \left(I_n^2 + I_{n,e}^2\right)^{1/2}, \quad (4)$$

where I_n and $I_{n,e}$ can be calculated as follows,

$$I_n = i_n \cdot \sqrt{B} \ , \quad (5)$$

$$I_{n,e} = e_n \cdot \frac{R_{sh}+R_f}{R_{sh} \cdot R_f} \cdot \sqrt{B} \ . \quad (6)$$

As can be observed, the noise level in the formulas is fully dependent on the bandwidth we are working with. By reducing the passing band of the system, we also reduce the noise level at the output. [11]

Use of step filters also reduces inter-channel interference, by limiting the input power of adjacent channels in the lock-in amplifiers. The main reason for introducing a filtering stage before the lock-in stage is to supply a strong and clean signal to the lock-in amplifier's input.

The practical bandwidth of the amplifier is limited by the time constant Rf·Cj, introduced by the union of the amplifier feedback resistor and the internal capacitance of the photodiode. Practical bandwidth can be calculated with the following formula. [26]

$$Bwp \approx \sqrt{\frac{GBp}{2 \cdot \pi \cdot R_f \cdot C_j}}, \quad (7)$$

where *Bwp* is the practical bandwidth; *GBp* is the gain/bandwidth product of the amplifier, *Rf* is the feedback resistor and *Cj* is the photodiode capacitance.

The amplifiers of the detectors are the AD745 and the AD549, with bandwidth/gain products of 20 and 1 MHz, while the photodiodes are the S5971 from Hamamatsu and the SPH203p from Osram, with capacitance values of 3pF and 11pF, respectively. For the detectors with the AD745 and the S5971 photodiodes, the practical bandwidth with a feedback resistor of 56MΩ value is 137.64 kHz. Using this value and setting the bandwidth of the filters to 100 Hz, we can calculate the effect that noise filters have on system performance. Calculating the quotient between the output noise level with filters and without them, we get a theoretical noise reduction value.

$$\frac{I_n^{Tot}unfiltered}{I_n^{Tot}filtered} = \frac{\left(I_n^2+I_{n,e}^2\right)^2}{\left(I_n^2+I_{n,e}^2\right)^2} = \frac{\sqrt{B_1}}{\sqrt{B_2}} = \sqrt{\frac{137.64kHz}{100Hz}} = 37 \text{ times less noise.}$$

In the case of the AD549 amplifier with the S5971 photodiode, the practical bandwidth is 25.4 kHz, using an 82 MΩ feedback resistor.

$$\frac{I_n^{Tot}unfiltered}{I_n^{Tot}filtered} = \frac{\left(I_n^2+I_{n,e}^2\right)^2}{\left(I_n^2+I_{n,e}^2\right)^2} = \frac{\sqrt{B_1}}{\sqrt{B_2}} = \sqrt{\frac{25.4kHz}{100Hz}} = 15.9 \text{ times less noise.}$$

4.3. Bandpass filter design process

There are many different configurations we can use to design a bandpass filter, including Sallen Key cells, Rauch cells, resonator configurations, low-pass / high-pass cascade union, etc. With some variants, each of them is highly dependent on the mathematical approach we use. Choosing one over the others depends on the initial specifications we want to achieve as well as the number of amplifiers available, implementation space and cost of manufacture. In our case, Sallen Key cells and low-pass/high-pass cascade unions were initially discarded due to the high number of stages, components and space needed to achieve high Q.

As already said, this application requires bandpass filters with central frequencies of 1, 2, 3 and 4 kHz as well as 6, 7, 8 and 9 kHz. Other requirements include a narrow passing band, no greater than 100 Hz, with maximum possible gain in the passing band and a minimum attenuation of 20 dB in the passing band of the other filters. The justification for using these close and low sets of frequencies is that, at the beginning, signal demodulation was made with LabVIEW software, and it was necessary to convert analog signals to digital ones using a data acquisition card with a limited sampling rate. To avoid losing information due to an insufficient sampling rate, channel frequencies were set to these values.

Two basic configurations were analyzed and compared before taking the final decision. The first configuration considered was a bandpass multi-feedback topology cell filter (MFB) or a Rauch topology cell filter with Butterworth coefficients, while the second circuit comprised a resonator bandpass filter, a special configuration that can be seen as a variant of the MFB. As a first step, a 1 kHz filter was designed and simulated to test both configurations.

4.3.1. MFB filter

Multi-feedback topology is one of the most common ones in bandpass filtering, because of ease of design, high quality factors and low number of components needed to implement it. Figure 10 shows the basic configuration of a second order filter.

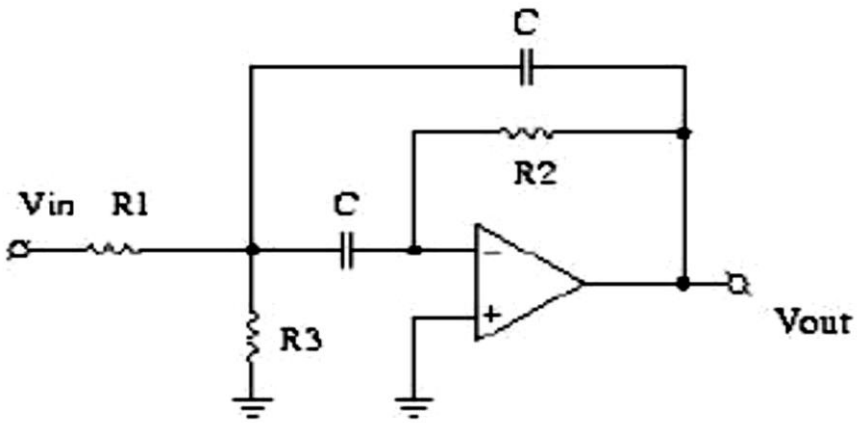

Figure 10. MFB filter topology.

The transfer function for this filter can be calculated by analyzing the circuit:

$$F(s) = \frac{\frac{-R_2 \cdot R_3}{R_1+R_3} \cdot C \cdot w_m \cdot s}{1+\frac{2 \cdot R_1 \cdot R_3}{R_1+R_3} \cdot C \cdot w_m \cdot s+\frac{R_1 \cdot R_2 \cdot R_3}{R_1+R_3} \cdot C^2 \cdot {w_m}^2 \cdot s^2} \quad , \tag{8}$$

where w_m is $2\pi fm$, and s is $j\omega$. Design equations can be derived from the transfer function:

$$f_m = \frac{1}{2 \cdot \pi \cdot C} \sqrt{\frac{R_1+R_3}{R_1 \cdot R_2 \cdot R_3}}, \tag{9}$$

$$A_m = \frac{-R_2}{2 \cdot R_1} \quad , \tag{10}$$

$$Q = \pi \cdot f_m \cdot R_2 \cdot C \quad , \tag{11}$$

$$B = \frac{1}{\pi \cdot R_2 \cdot C} \quad . \tag{12}$$

Our design was a fourth-order filter, fabricated by connecting two MFB second-order filters and using the Butterworth model to approximate the transfer function due to maximum flatness. Being a product of two transfer functions, the total transfer

function is shown in Figure 11 and Table 1 presents the coefficients needed for the calculations.

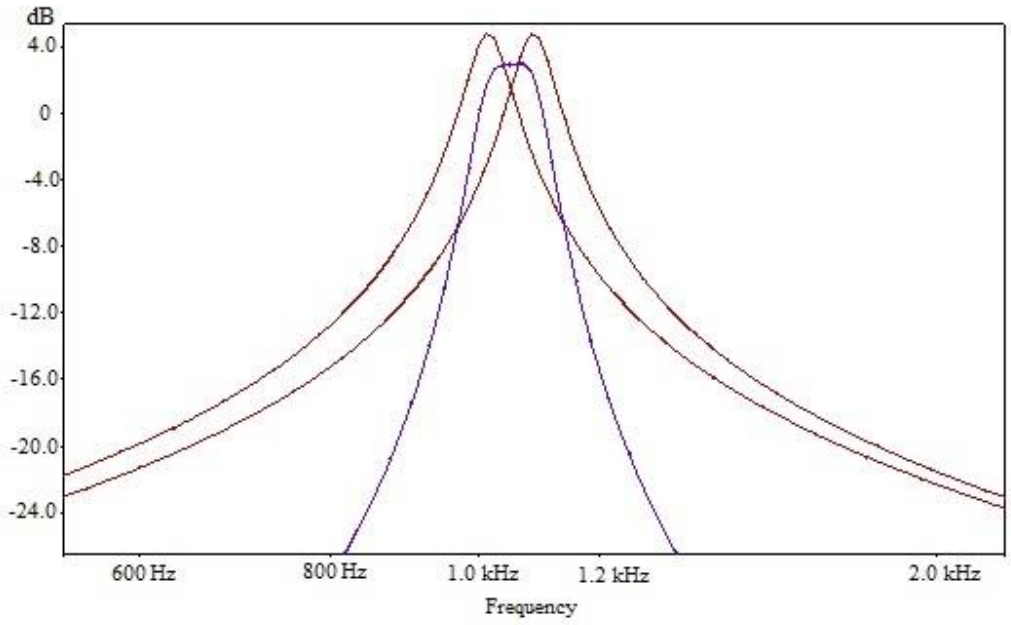

Figure 11. Transfer functions of the second-order filters (in black) and the resulting fourth-order filter (in blue).

Table 1. Butterworth coefficients for MFB filter design

Butterworth			
a1	1.14142		
b1	1.0000		
Q	100	10	1
α	1.0035	1.036	1.4426

The fourth-order MFB filter has the following transfer function:

$$F(s) = \frac{\frac{A_{mi}}{Q_i}.\alpha \cdot s}{[1+\frac{\alpha \cdot s}{Q_1}+(\alpha \cdot s)^2]} \cdot \frac{\frac{A_{mi}}{Q_i}.\frac{s}{\alpha}}{[1+\frac{\alpha \cdot s}{Q_1}+(\frac{s}{\alpha})^2]} \quad , \qquad (13)$$

where A_{mi} is the gain of each stage at the central frequency, Q_i the quality factor of the stages and α and $1/\alpha$ the drift factor of the central frequency of the second-order

filters with respect to the central frequency of the fourth-order filter. This factor is calculated by numerical methods, and Table 1 shows a tabulated value for each mathematical approximation and for each quality factor. The following equations will be used to calculate a specification for each stage to achieve a global specification:

$$f_{m1} = \frac{f_m}{\propto}\,, \tag{14}$$

$$f_{m2} = f_m \cdot \alpha\,, \tag{15}$$

$$Q_i = Q \cdot \frac{(1+\alpha^2)\cdot b_1}{\propto \cdot a_1}\,, \tag{16}$$

$$A_{mi} = \frac{Q_i}{Q} \cdot \sqrt{\frac{A_m}{b_1}}\,, \tag{17}$$

where f_{m1} and f_{m2} are the central frequencies of each stage, with all other parameters as in the previous paragraph. To summarize, we are going to design a fourth-order MFB filter using the Butterworth mathematical approximation. In essence, this filter consists of two stages, each comprising a second-order band-pass MFB filter. The starting point of the design consists of our final specifications, $f_m = 1000Hz$ and $Q = 10$, giving us a bandwidth of 100Hz and a total gain A_m, which was initially set to 2 (3dB of gain). Substituting these values and those for Q=10 with values obtained from the Butterworth approximation, namely $a_1 = 1.14142$, $b_1 = 1$, $\propto = 1.036$, we get a set of specifications for second-order filters:

$$f_{m1} = \frac{f_m}{\propto} = \frac{1000Hz}{1.036} = 965.25Hz$$

$$f_{m2} = f_m \cdot \alpha = 1000 \cdot 1.036 = 1036Hz$$

$$Q_{1,2} = Q \cdot \frac{(1+\alpha^2)\cdot b_1}{\propto \cdot a_1} = \frac{(1+1.036^2)\cdot 1}{1.036 \cdot 1.14142} = 17.53$$

$$A_{m1,2} = \frac{Q_{1,2}}{Q} \cdot \sqrt{\frac{A_m}{b_1}} = \frac{17.53}{10} \cdot \sqrt{\frac{2}{1}} = 2.4$$

Using the following values for the first stage: $f_{m1} = 965.25Hz$, $Q_1 = 17.53$ and $A_{m1} = 2.48$, and fixing the capacitor value at 100nF, we may calculate resistor values from the design formulas for second-order band-pass MFB filters:

$$Q = \pi . f_m . R_2 . C \;\rightarrow\; R_2 = \frac{Q}{\pi . f_m . C} = \frac{17.53}{\pi \cdot 965.25 \cdot 100 \cdot 10^{-9}} = 55799.7 \approx 55.8k\Omega$$

$$|A_m| = \frac{R_2}{2.R_1} \;\rightarrow\; R_1 = \frac{R_2}{2 \cdot |A_m|} = \frac{55799.7}{2 \cdot 2} = 13949.9 \approx 14k\Omega$$

$$f_{m1} = \frac{1}{2\pi C}\sqrt{\frac{R_1 + R_3}{R_1 . R_2 . R_3}} \;\rightarrow$$

$$R_3 = \frac{1}{R_2 \cdot \left((2\pi \cdot f_{m1} \cdot C)^2 - \frac{1}{R_1 \cdot R_2}\right)} = \frac{1}{55799.7 \cdot \left((2\pi \cdot 965.25 \cdot 100 \cdot 10^{-9})^2 - \frac{1}{13949.9 \cdot 55799.7}\right)} \approx 49\Omega$$

Using the same procedure for the second stage with the following values: $f_{m2} = 1036Hz$, $Q_1 = 17.53$, $A_{m1} = 2.48$ and $C = 100nF$, we get the corresponding resistor values:

$$R_{22} = \frac{Q}{\pi . f_{m2} . C} = \frac{17.53}{\pi \cdot 1036 \cdot 100 \cdot 10^{-9}} = 53860.7 \approx 54k\Omega$$

$$R_{11} = \frac{R_{22}}{2 \cdot |A_m|} = \frac{53860.7}{2 \cdot 2} = 13465.1 \approx 13.5k\Omega$$

$$R_{33} = \frac{1}{R_{22} \cdot \left((2 \cdot \pi \cdot f_{m2} \cdot C)^2 - \frac{1}{R_{11} \cdot R_{22}}\right)}$$

$$= \frac{1}{53860.7 \cdot \left((2\pi \cdot 1036 \cdot 100 \cdot 10^{-9})^2 - \frac{1}{13465.1 \cdot 53860.7}\right)} \approx 44\Omega$$

Having obtained these values, the design is complete, and the resulting circuit, drawn in OrCAD, is shown in Figure 12.

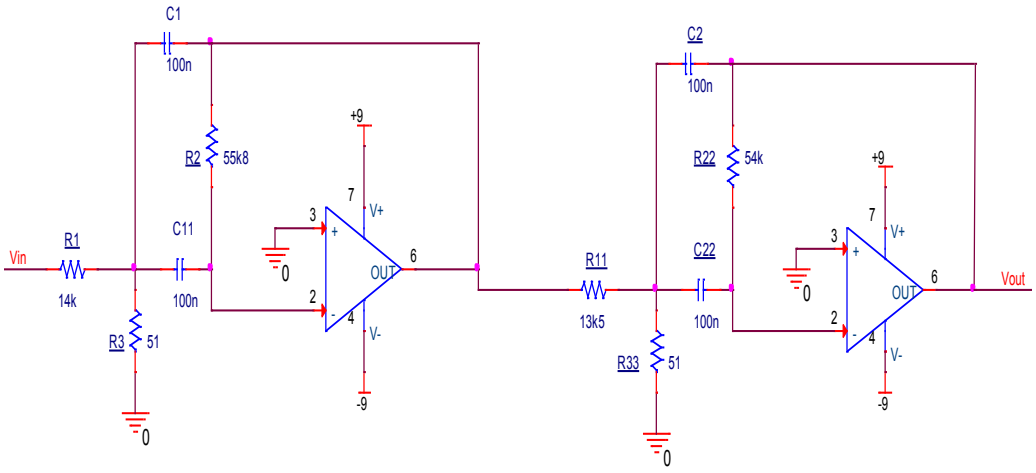

Figure 12. Schematic of the fourth-order MFB filter for 1 kHz.

Figure 13 presents a simulation result for this schematic.

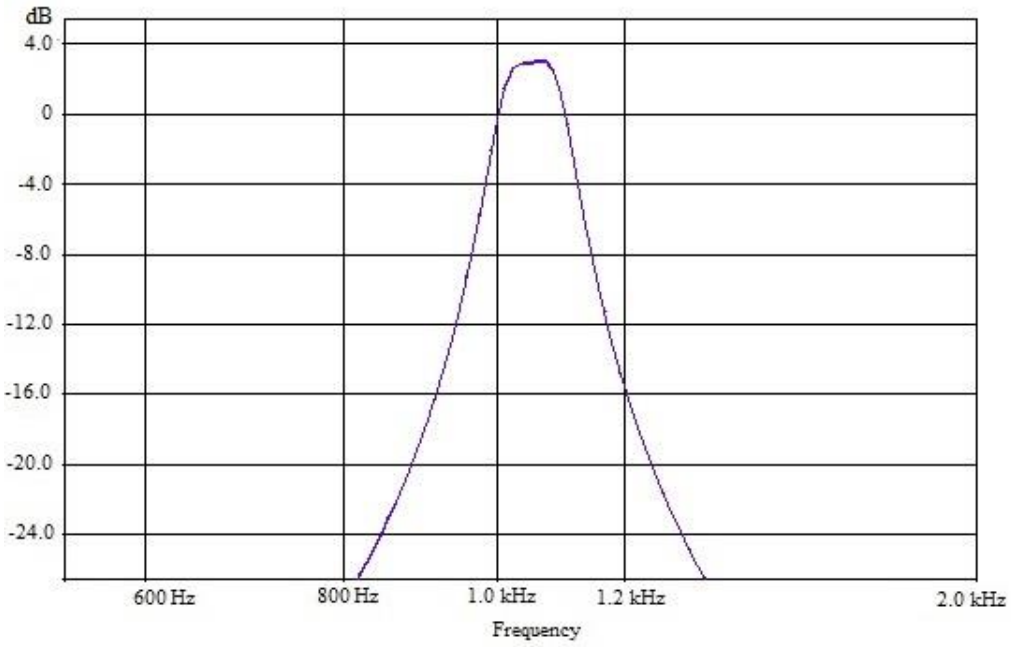

Figure 13. Transfer function of the fourth-order MFB filter.

As shown in Figure 13, the central frequency is not fully centered at 1 kHz and no gain is present at this point. However, this can be fixed by adjusting the resistors R3 and R33 to move the central peaks of the second-order filters. After some tests and simulations, we get the transfer functions shown in Figure 14, for R3=51Ω and R33=51Ω.

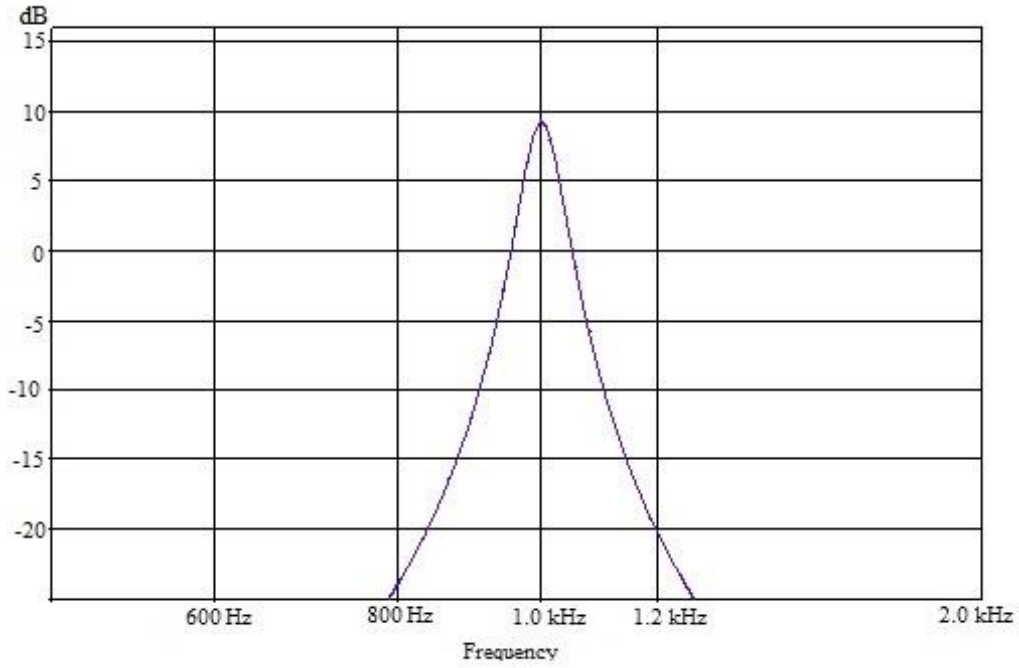

Figure 14. Adjusted transfer function of the fourth-order MFB filter.

This filter has better attributes than the one designed earlier. Its quality factor $Q = 13.92$, bandwidth $B = 44.659$ Hz at -3dB and maximum gain in the passing band $A_m = 9.36\, dB$. Moreover, attenuation of the nearest channel (2 kHz) is around 44dB, which is two times more than the desired attenuation, although the central frequency is very sensitive to changes in R3 and R33.

4.3.2. Resonator filter

Less well-known and used than the MFB topology, the resonator configuration gives good results, while being easier to design. In addition, it allows easier adjustment of parameters. The basic configuration is shown in Figure 15.

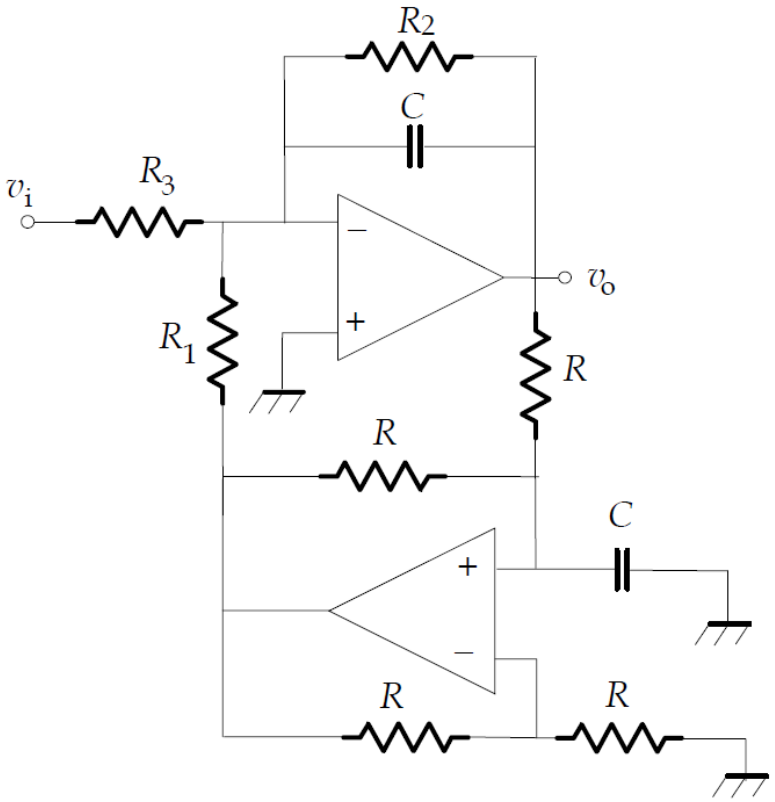

Figure 15. Basic configuration of a resonator filter.

The transfer function of the circuit is the following one,

$$F(s) = \frac{\frac{-R_2}{R_3}\cdot C\cdot s}{R_2\cdot C^2\cdot s^2 + C\cdot s - \frac{2.R_2}{R_1\cdot R}}, \tag{18}$$

This equation reveals that for a fixed value of R2, R and C, the gain of the circuit is controlled by R3, while the central frequency can be adjusted with the resistor R1.

Design equations are the following:

$$R = \frac{1}{2\pi\cdot f_m\cdot C}, \tag{19}$$

$$R_1 = \frac{1}{\pi\cdot f_m\cdot C}, \tag{20}$$

$$R_2 = \frac{1}{2\pi\cdot C\cdot B}, \tag{21}$$

$$R_3 = \frac{1}{2\pi\cdot C\cdot B\cdot G}. \tag{22}$$

The specifications used for designing the filter were $f_m = 1kHz, B = 100Hz$, $g = 2$, and the capacitors were fixed to 100 nF. Using these specifications, we get the following resistors values:

$$R = \frac{1}{2\pi \cdot f_m \cdot C} = \frac{1}{2\pi \cdot 1000 \cdot 100 \cdot 10^{-9}} = 1591.5\ \Omega \approx 1592\ \Omega$$

$$R_1 = \frac{1}{\pi \cdot f_m \cdot C} = \frac{1}{\pi \cdot 1000 \cdot 100 \cdot 10^{-9}} = 3183\ \Omega$$

$$R_2 = \frac{1}{2\pi \cdot C \cdot B} = \frac{1}{2\pi \cdot 100 \cdot 10^{-9} \cdot 100} = 15915.4\ \Omega \approx 15915\ \Omega$$

$$R_3 = \frac{1}{2\pi \cdot C \cdot B \cdot G} = \frac{1}{2\pi \cdot 100 \cdot 10^{-9} \cdot 100 \cdot 2} = 7957.7\ \Omega \approx 7958\ \Omega$$

With these values, the design process is complete. A schematic of the circuit is shown in Figure 16.

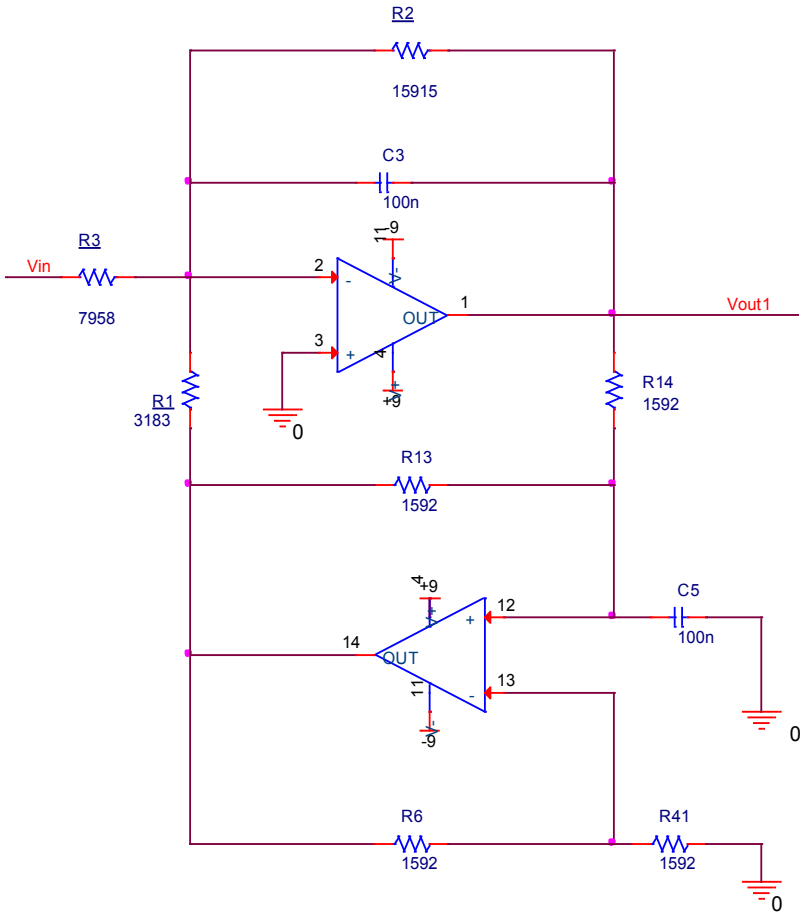

Figure 16. Schematic of the resonator filter for 1 kHz.

The transfer function of the circuit is shown in Figure 17.

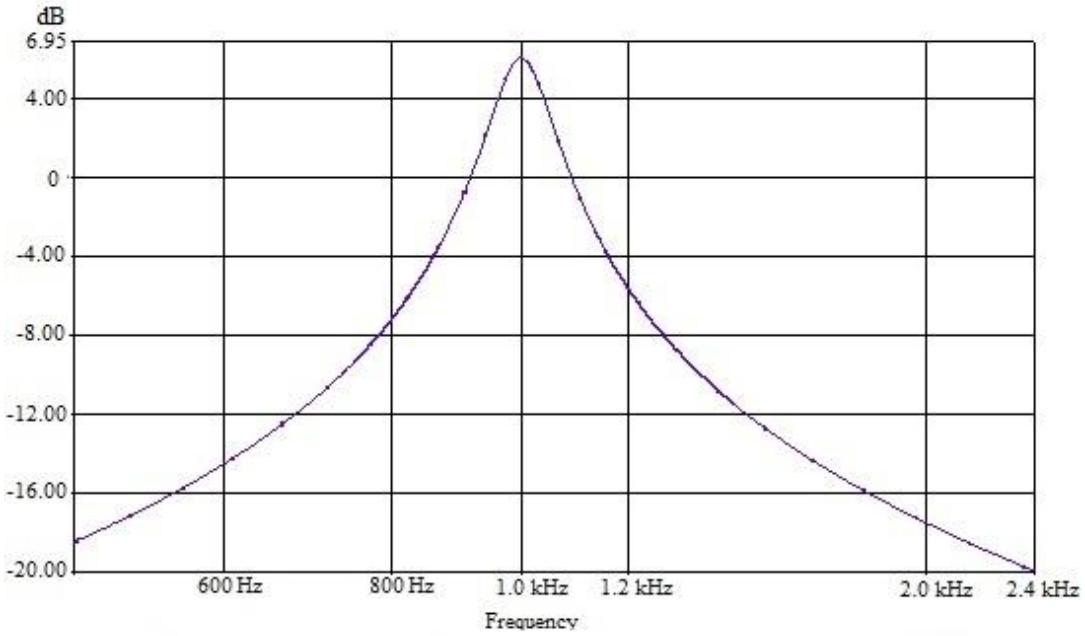

Figure 17. Transfer function of the resonator filter.

The circuit's quality factor $Q = 9.87$, bandwidth $B = 98.65Hz$ and gain in the central frequency $A_m = 6.11dB$. Although these parameters are in the range we were looking at, attenuation in the adjacent channel (2 kHz) is less than 20dB. To improve that figure, the bandwidth was reduced by doubling the values of R2 and R3. The resulting transfer function of the circuit is shown in Figure 18.

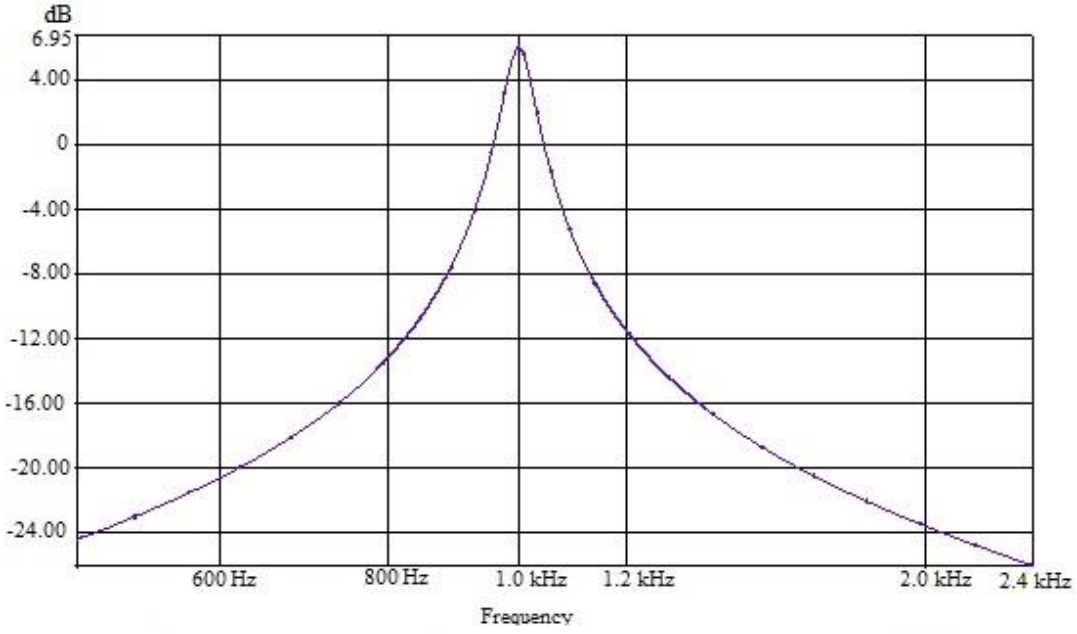

Figure 18. Final transfer function of the resonator filter.

After changing resistor values, the final characteristics of the resonator filter are these: quality factor $Q = 19.57$, bandwidth $B = 48.59Hz$, gain in the central frequency $A_m = 6.21dB$ and attenuation in the adjacent channel is -23.5 dB. Thus, by making a small change to the initial design, we get the desired filter properties. Compared with the MFB, the advantage of this filter is that gain, central frequency and bandwidth can be separately adjusted by tweaking one or two components. Although the MFB approach is more complicated, due to the two stages and the resultant parameter interdependence, it nevertheless offers better characteristics. Thus, it seems a better solution for the final device with a fixed central frequency value. Figure 19 provides a comparison of both transfer functions.

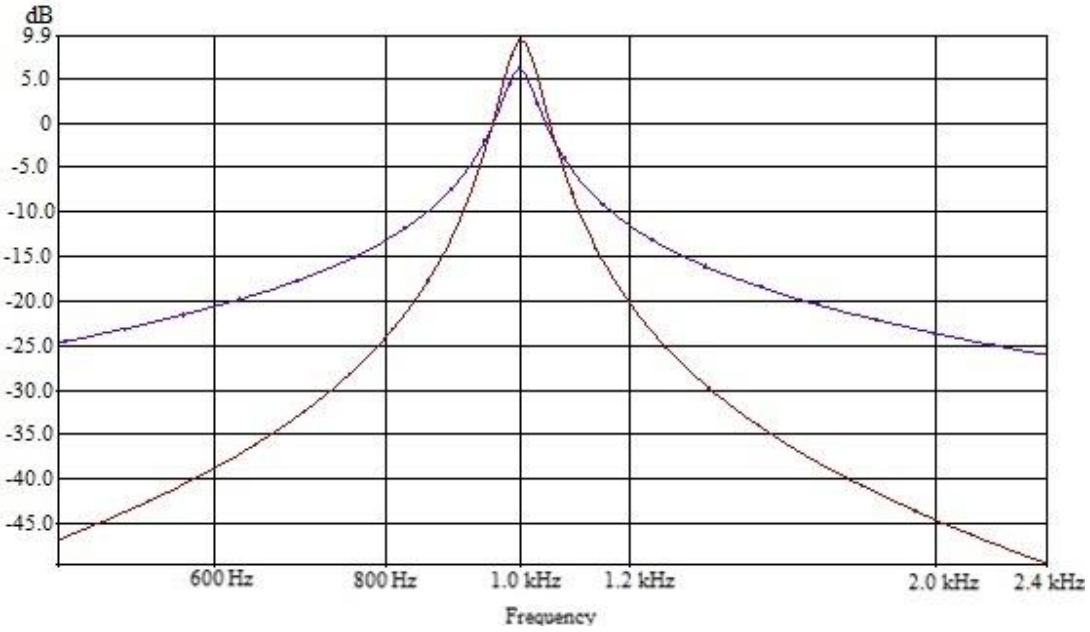

Figure 19. Transfer functions of the MFB filter (red) and the resonator filter (blue).

Ultimately, we decided to implement the resonator filter, because it is used in the test prototype of the NIR device, although not in the final version. Our intention was to examine a range of configurations with different channels (frequencies) during the testing process, so the availability of easily tunable filters was of essence. The central peak of the resonator filter's transfer function can be shifted to other frequencies without changing its shape, and gain can also be adjusted within a specific range without changing the central frequency. To achieve this, R1 and R3 were substituted by trimmers. Figure 20 shows the transfer function of the resonator filter designed for 1 kHz (Figure 16). Only the value of R1 has been changed and set to 100 Ω , instead of 3183 Ω , which was the value used in the original calculations.

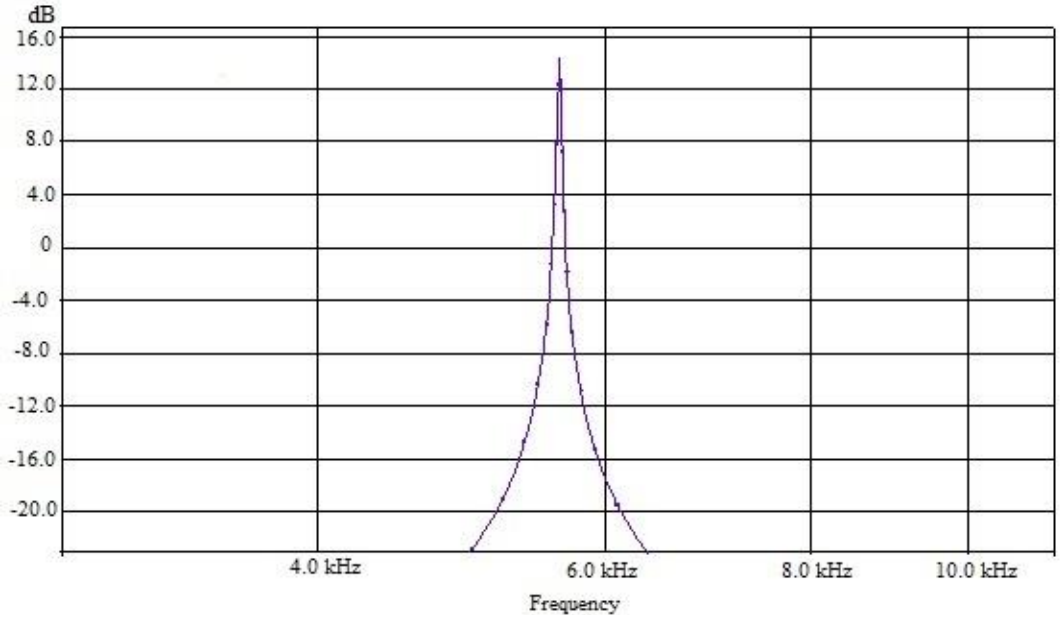

Figure 20. Transfer function of the shifted 1kHz filter with $R_1 = 100\Omega$.

As indicated by Figure 20, by lowering the value of resistor R_1, the central frequency shifts to almost 6 kHz. Beyond this point, gain starts decreasing very fast, and at 8 kHz attenuation is too high for the filter to be used in the intended application. It seems that gain increased only in the simulation, but in the real world.

4.4. Physical implementation of the filters

At the first step, four filters were designed and implemented, as this was the number of channels used in the NIR device. Although designed with a central frequency of 1, 2, 3 and 4 kHz, respectively, the filters also came with the added ability to change frequency. Their bandwidths were initially set to 100 Hz, but after a set of simulations, they were changed to achieve the right amount of attenuation in adjacent channels, as described earlier. In theoretical calculations during the design process, we used a bandwidth of 60 Hz and a gain of 2. Table 2 presents values calculated for the components of each filter according to the schematic in Figure 16.

Table 2. Component values for resonator filters

Central frequency	R	R1	R2	R3	C
1000Hz	1592Ω	3183Ω	26526Ω	13262Ω	100nF
2000Hz	796Ω	1592 Ω	26526Ω	13262Ω	100nF
3000Hz	531 Ω	1062 Ω	26526Ω	13262Ω	100nF
4000Hz	398 Ω	796 Ω	26526Ω	13262Ω	100nF

Normalized values for standard E24 resistors and capacitors and for components available in the laboratory are shown in Table 3.

Table 3. Normalized component values for resonator filters

Central frequency	R	R1 Trimmer	R2	R3 Trimmer	C
1000Hz	1600Ω	MAX 5000Ω	27300Ω	MAX 50kΩ	100nF
2000Hz	820 Ω	MAX 5000Ω	27300Ω	MAX 50kΩ	100nF
3000Hz	510 Ω	MAX 5000Ω	27300Ω	MAX 50kΩ	100nF
4000Hz	390 Ω	MAX 2000Ω	27300Ω	MAX 50kΩ	100nF

Shown in Figure 21 are the transfer functions of the filters, with the normalized values for the resistors and trimmers set to the calculated values.

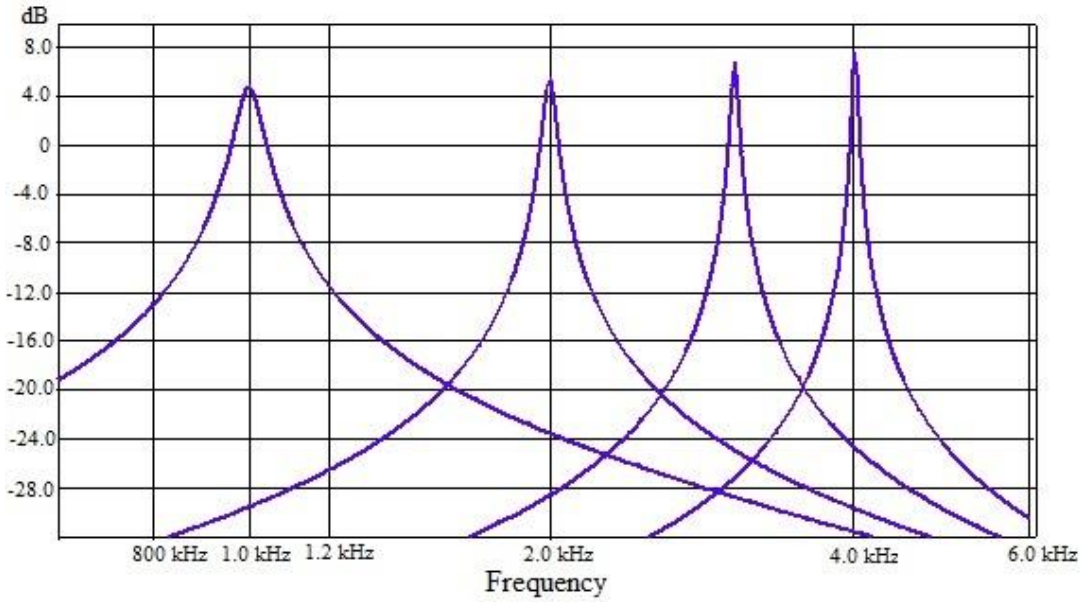

Figure 21. Transfer function of the filters with the normalized resistor.

Circuit schematics and the PCB were designed with Eagle software. The amplifier used in the circuit was the TCL2274CN from Texas Instruments, which contains four operational amplifiers. Two chips were used to construct the filters, with two amplifiers for each filter, making a total of 8 amplifiers. Voltage regulators were added to the circuit to avoid voltage changes in the amplifiers' power lines and to provide additional filtering for high frequencies in the voltage supply lines. Figure 22 presents a schematic of the circuit:

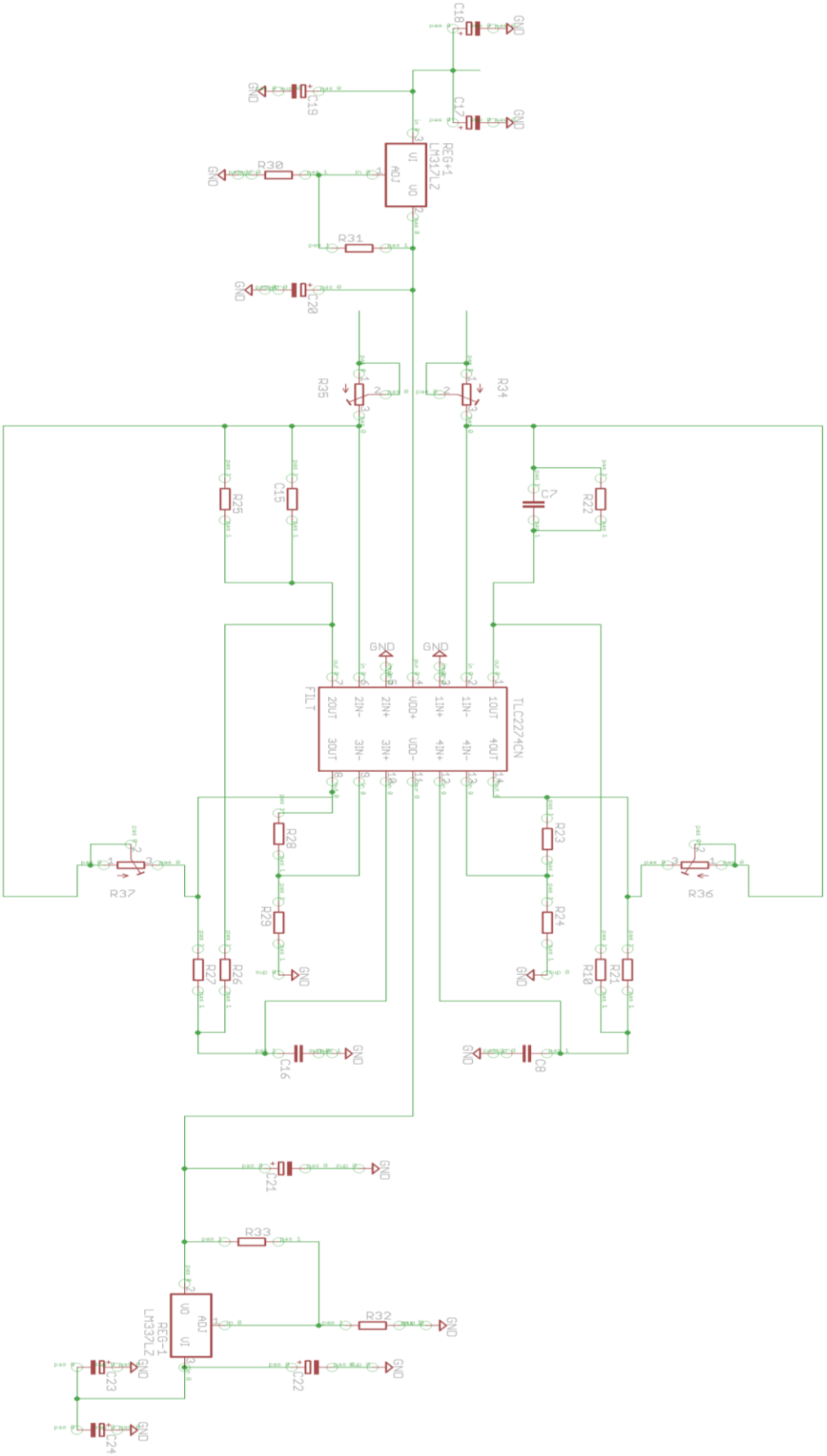

Figure 22. Eagle schematic for two filters.

This circuit was placed twice on the same PCB, as illustrated in Figures 23 and 24, showing the final PCB layout.

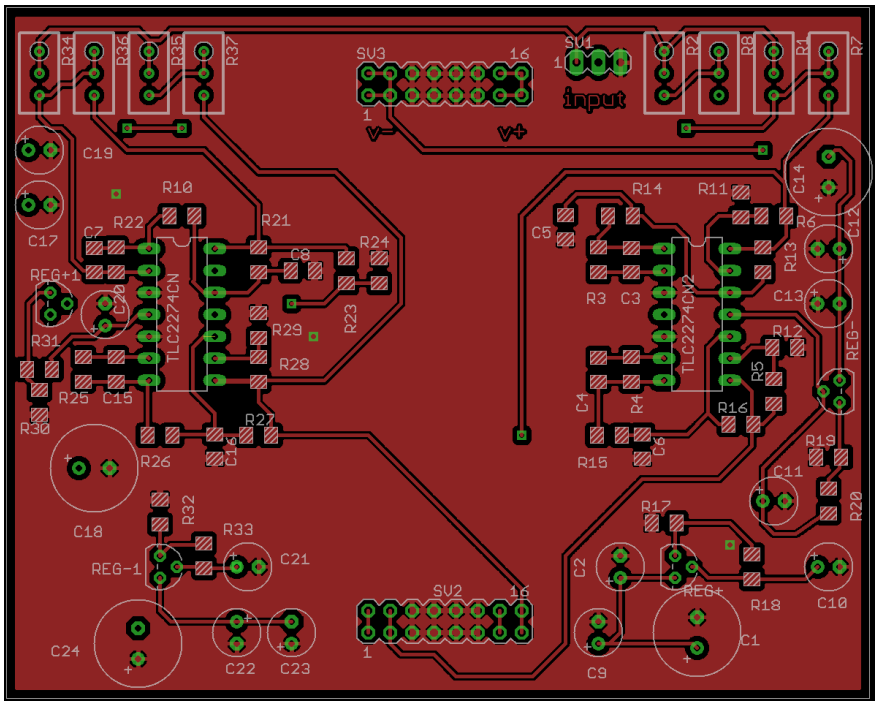

Figure 23. Top layer of the filter PCB.

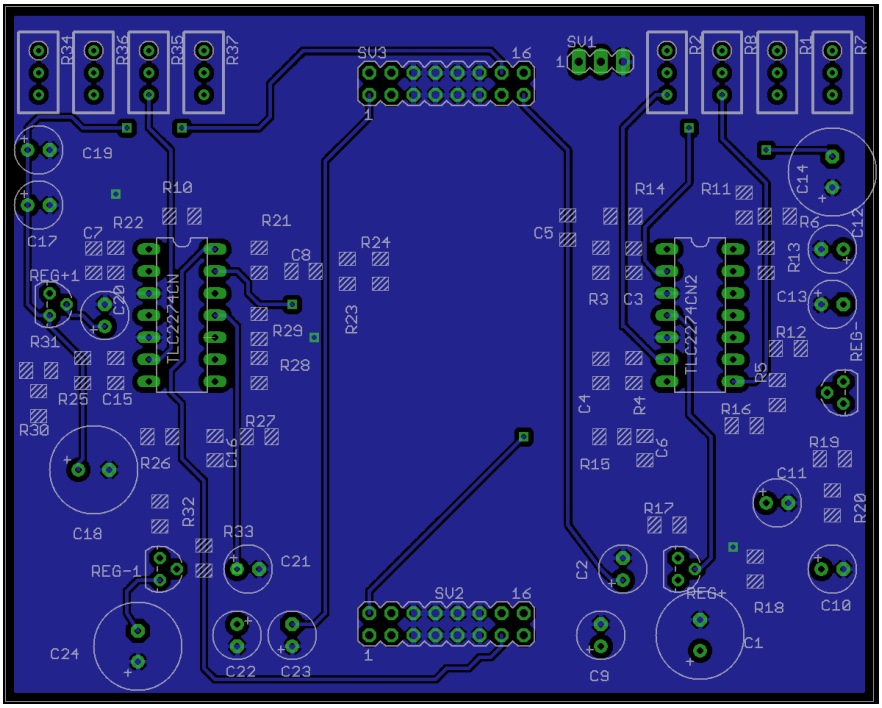

Figure 24. Bottom layer of the filter PCB.

The PCB was manufactured in the workshop of the University of Oulu. Assembly and soldering of components were done by the author in the Optoelectronics and Measurement Techniques Laboratory of the university.

After testing and adjusting the board, the research group decided to keep using the existing frequencies, i.e., 6, 7, 8 and 9 kHz, to avoid having to change the whole system. This was due to ongoing collaboration with the Oulu University Hospital, who needed a working NIR system for clinical work. However, this first circuit was useful for the development of the other filters and served as a base for future improvements.

A second set of filters was constructed using the same schematic, but with central frequencies of 6, 7, 8 and 9 kHz. Filter design consisted of calculating new values for the components, running simulations in ORCAD using normalized components and performing the same manufacturing process, including soldering and assembly. This time, 3 groups of 4 filters (6, 7, 8, 9 kHz) were implemented on two PCBs (24 filters) to enable expanding the number of detectors being used at the same time, for example, to make multidistance measurements. The schematic shown in Figure 22 was replicated 6 times on the same PCB. Table 4 presents calculated values for all components.

Table 4. Calculated values for resonator filter components

Central frequency	R	R1	R2	R3	C
6000Hz	1205Ω	2410Ω	103kΩ	51kΩ	22nF
7000Hz	1033Ω	2066 Ω	103kΩ	51kΩ	22nF
8000Hz	904 Ω	1808 Ω	103kΩ	51kΩ	22nF
9000Hz	803 Ω	1606Ω	103kΩ	51kΩ	22nF

Filter bandwidth was set to 70 Hz, instead of 60 Hz, to prevent resistors R2 and R3 from increasing too much. Excessively high resistor values restrain currents from flowing properly, changing circuit behavior too much, when tuning the filters. It is also important to note that capacitors with smaller capacitance were selected to avoid the use of small resistances in R and R1, which would add instability to the circuit. In addition, small resistances complicate filter tuning and make components more expensive. The Table 5 shows the final normalized values.

Table 5. Selected normalized values for resonator filter components

Central frequency	R	R1 Trimmer	R2	R3	C
6000Hz	1200Ω	5kΩ	100kΩ	43kΩ	22nF
7000Hz	1010Ω	5k Ω	100kΩ	43kΩ	22nF
8000Hz	910 Ω	5kΩ	100kΩ	43kΩ	22nF
9000Hz	820 Ω	2k Ω	100kΩ	43kΩ	22nF

The resistor R3 was a bit smaller to increase amplification and to compensate for errors committed when selecting the other components. Figures 25 and 26 illustrate the PCB layout.

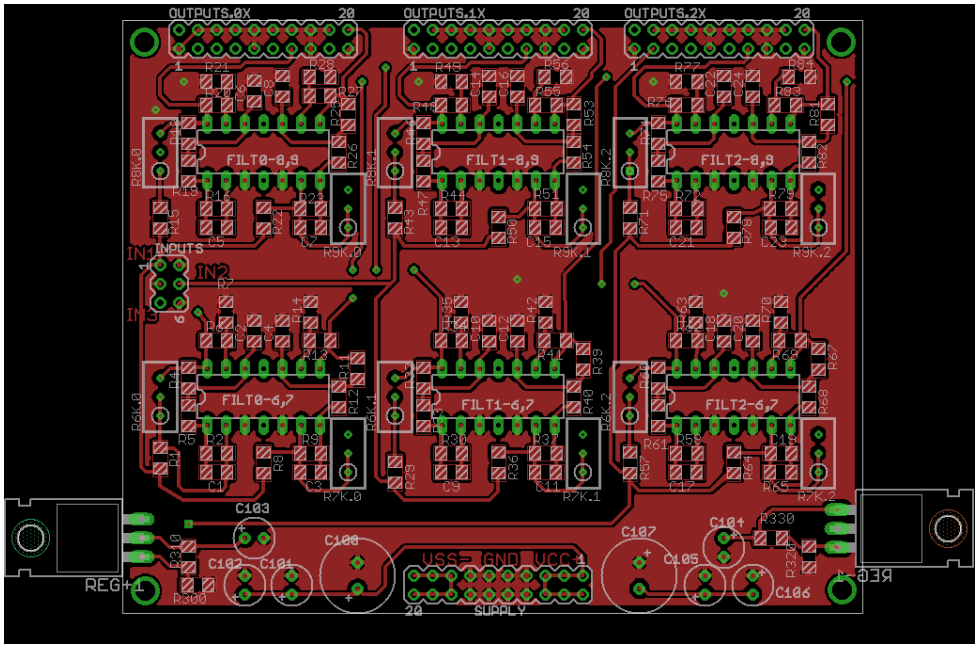

Figure 25. Top layer of the filter PCB.

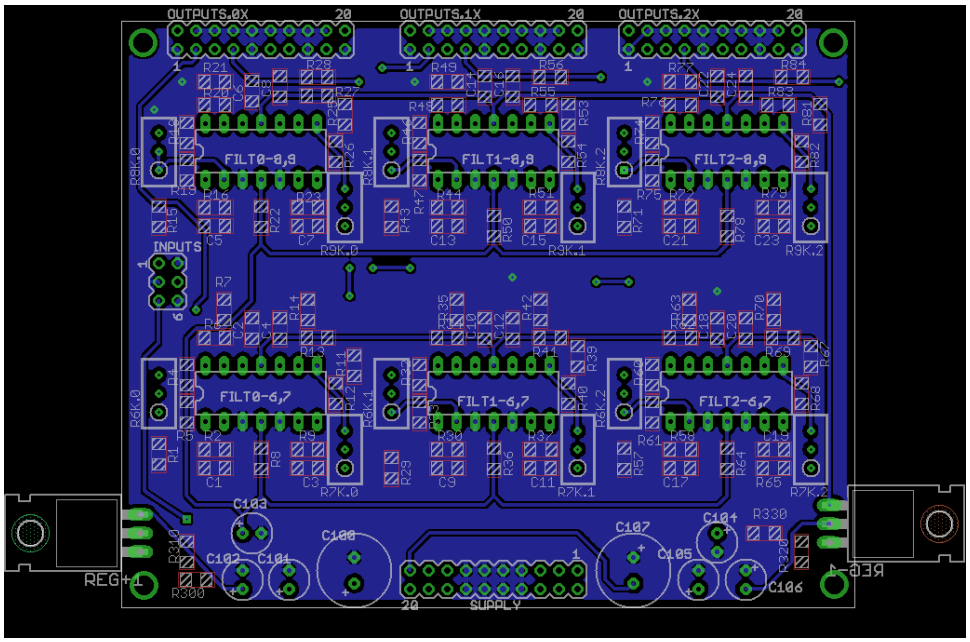

Figure 26. Top layer of the filter PCB.

Figure 27 shows the first PCB, with the filters centered on 1, 2, 3 and 4 kHz in the testing cage.

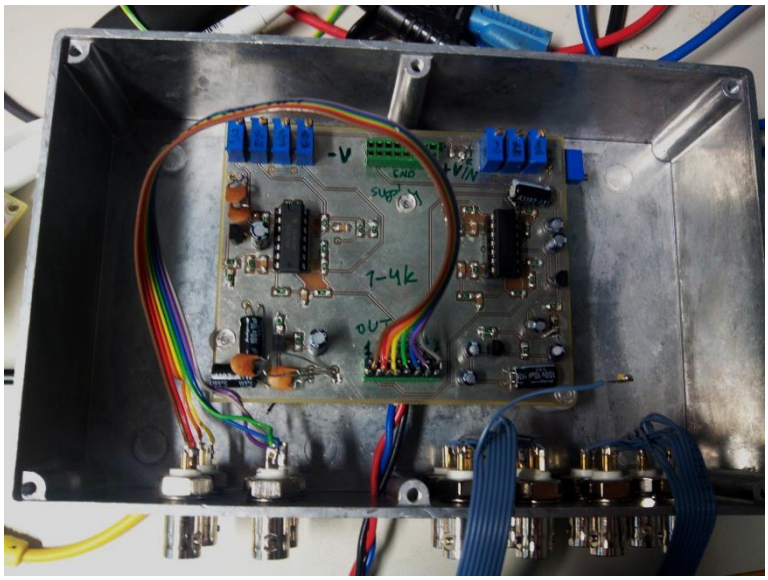

Figure 27. Picture of the filter PCB for 1, 2, 3 and 4 kHz.

Figure 28 shows a photo of the second set of filters. Two PCBs were made, each containing 12 filters, 3 for each frequency (6, 7, 8, 9 kHz). These PCBs were prepared for insertion within the NIR device and connected to its subsystems by flat cables. Corners of the PCBs were drilled to allow attachment to the chassis of the prototype.

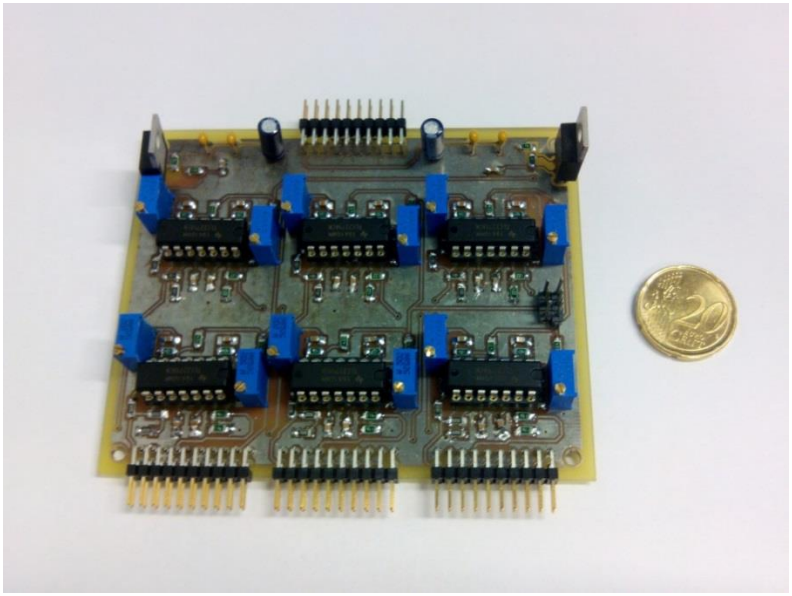

Figure 28. Picture of the filter PCB for 6, 7, 8 and 9 kHz.

Supply voltage in all circuits was the same as in the NIR device, ±12V, and the amplifiers were fed with ±10V, so the regulators were calculated to convert ±12V to ±10V with a stable value. The designed regulators use the LM317LZ chip to convert +12V to +10V and the LM337LZ chip to convert -12V to -10V. The configuration is shown in Figure 29.

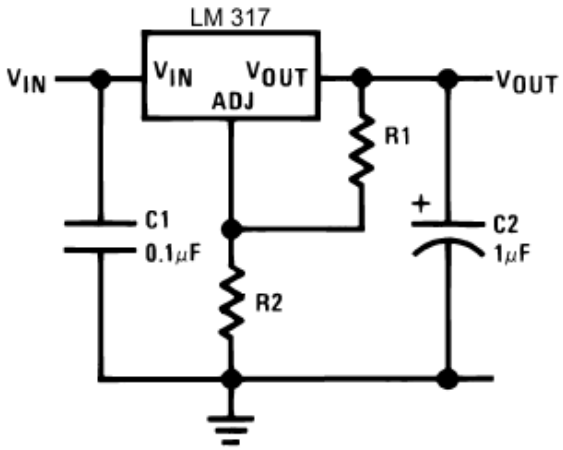

Figure 29. Positive regulator.

Component values were set with the following formula,

$$V_{out} = 1.25 \cdot \left(1 + \frac{R_2}{R_1}\right) + (I_{ADJ} \cdot R2). \quad (23)$$

The value of I_{ADJ} is around 100μA, so the term on the right side of the equation can be neglected. The value of R_2 can be calculated with this formula, and fixing the value of $R_1 = 130\Omega$, we get

$$R_2 = \left(\frac{V_{out}}{1.25} - 1\right) \cdot R_1 = \left(\frac{10V}{1.25} - 1\right) \cdot 130 = 910\Omega.$$

Normalized values for the standard E24 resistors are $R_1 = 130\Omega$ and $R_2 = 910\Omega$. Capacitors C1 and C2 are provided for additional stability, and their values are those recommended by the manufacturer. For the negative voltage, the circuit used is that shown in Figure 30.

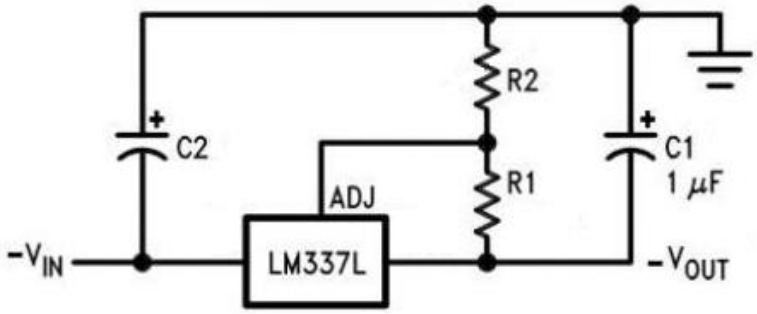

Figure 30. Negative regulator.

According to the manufacturer, the formula to calculate resistor values is

$$-V_{out} = -1.25 \cdot \left(1 + \frac{R_2}{R_1}\right). \quad (24)$$

The value of R_2, when R_1 has a fixed value of 130Ω, is:

$$R_2 = \left(\frac{V_{out}}{1.25} - 1\right) \cdot R_1 = \left(\frac{10V}{1.25} - 1\right) \cdot 130 = 910\Omega.$$

As for the positive regulator, normalized values for standard E24 resistors are $R_1 = 130\Omega$ and $R_2 = 910\Omega$. Two capacitors, C1 and C2, are used for additional stability and, as their values are those recommended by the manufacturer, C2 has a value of 10μF.

4.4.1. Practical Results

After implementation of the circuits, several tests were run to ensure that the filters were working properly. Their transfer function was checked and measured with an oscilloscope. Figure 31 shows a simulated and measured transfer function for the 1 kHz filter. For the measured transfer function, a 1 V peak-to-peak pure tone was generated and fed to the input of the filter, with its output directly connected to the oscilloscope. The frequency of the tone was manually shifted from 100 Hz to 2000 Hz. All in all, 205 points were measured, although not in a linear way, and introduced to MatLab to draw the transfer function.

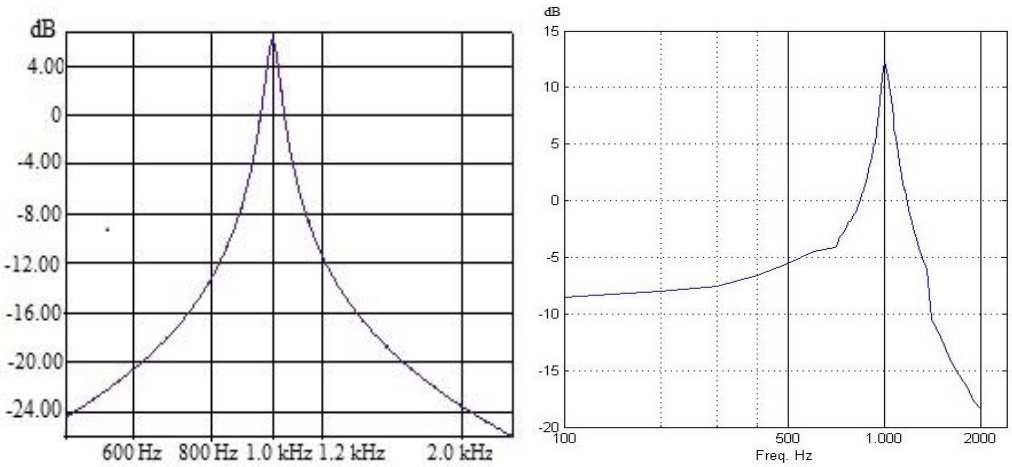

Figure 31. Simulated (left) and real transfer function (right) of the 1 kHz filter.

As shown in the figures, real filter behavior is quite similar to the simulated response. Near the central frequency in particular, the transfer function is almost identical with the ideal one. Moreover, attenuation of the adjacent channel, i.e., 2 kHz, is very close to 20 dB (around 19dB), which is a remarkably good result, considering the use of normalized values and the tolerance of the real components as well as the shortcomings of the measurement system. It is also noteworthy that for frequencies lower than 100 Hz, the slope falls very quickly and, at 0 Hz, attenuation is very high.

Several tests were conducted on the other filters with very similar results. With minor differences in filter characteristics, they all lie in the valid tolerance range for the intended application. Figure 32 shows how the 6 kHz filter reconstructs a signal detected through a finger:

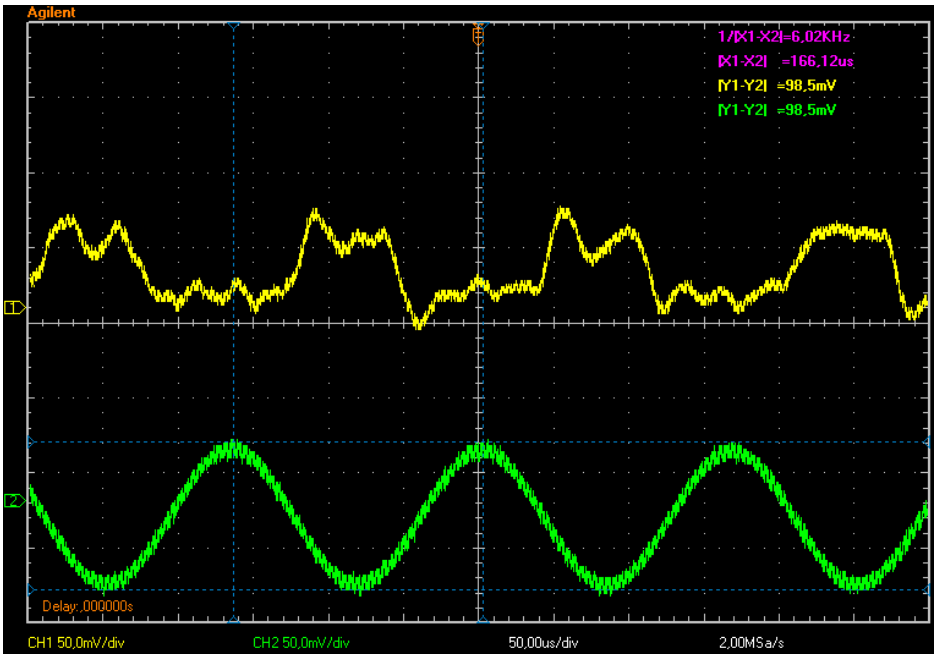

Figure 32. Unfiltered signal (upper signal) vs. filtered signal (lower signal).

In this case, the finger was illuminated with red light having a wavelength of 660 nm, modulated with a pure 6 kHz signal. The light source was placed on one side of the finger and the detector on the other. In the figure, the upper signal is the one detected by the light detector, which was also designed in this thesis. Being very noisy, this signal is of little use. The lower signal, on the other hand, represents the very same signal after filtering by the designed 6 kHz filter. Modulation of the signal is now clearly visible and, when demodulated using the lock-in technique, the signal reveals fluctuations in light attenuation as a function of amplitude changes.

Figure 33 presents another example of the efficiency of the filters. In this case, the forehead of a collaborator was illuminated with NIR light modulated by a pure tone with a frequency of 8 kHz. A detector was placed at a distance of 3 cm from the light source. The upper signal was measured right after the detector and the lower one after the filters.

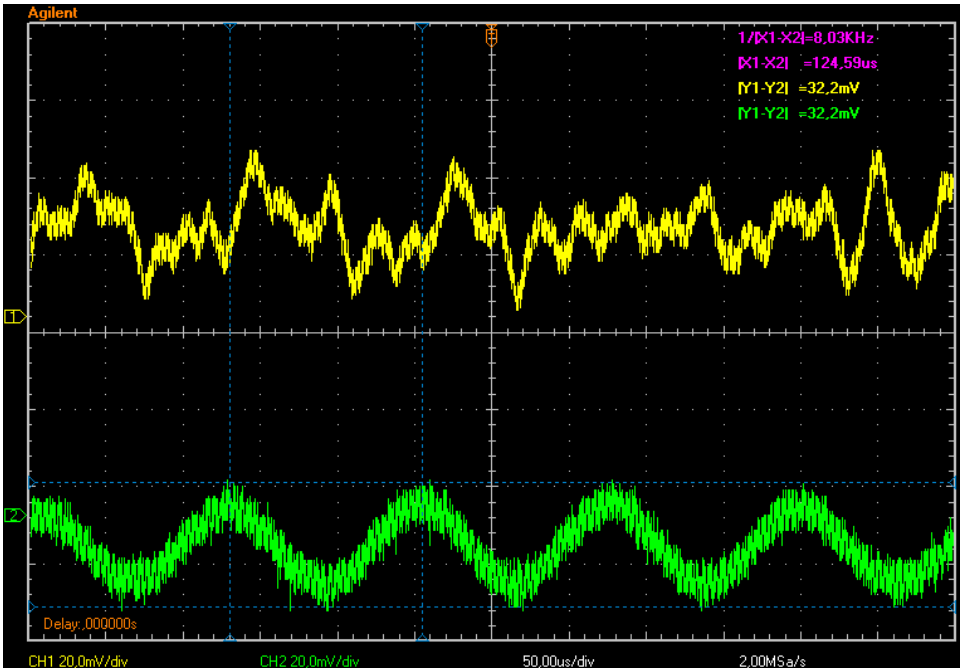

Figure 33. Unfiltered signal (upper signal) vs. filtered signal (lower signal).

As shown in Figure 33, it is hard to find any periodicity in the detected signal, but after the filter, we have an 8 kHz clear tone, even when the level of the input signal is less than 30 millivolts. Similar results were obtained from the others filters with different setups. In terms of their intended purpose, we thus got very good results for the filters.

5. LIGHT DETECTORS

The following sections provide a brief study of the basic principles and technology of light detection, offering a first step toward understanding the work conducted here. These sections will be followed by a detailed description of the work, before concluding the thesis with a presentation of the most salient results.

5.1. Introduction to light detection

Light has a dual nature and can be treated either as a wave or a flux of particles [27, 28]. This thesis focuses on light as a particle phenomenon, consisting of a group of particles called photons.

Most light detectors are based on the photoelectric effect, which can be described in a simple way as follows. When a stream of photons with enough energy, such as a beam of light, impacts a material, it creates a flux of electrons moving away from the material. This effect can be used to convert the energy of the light to an electrical current [28]. Figure 34 shows a schematic of the photoelectric effect.

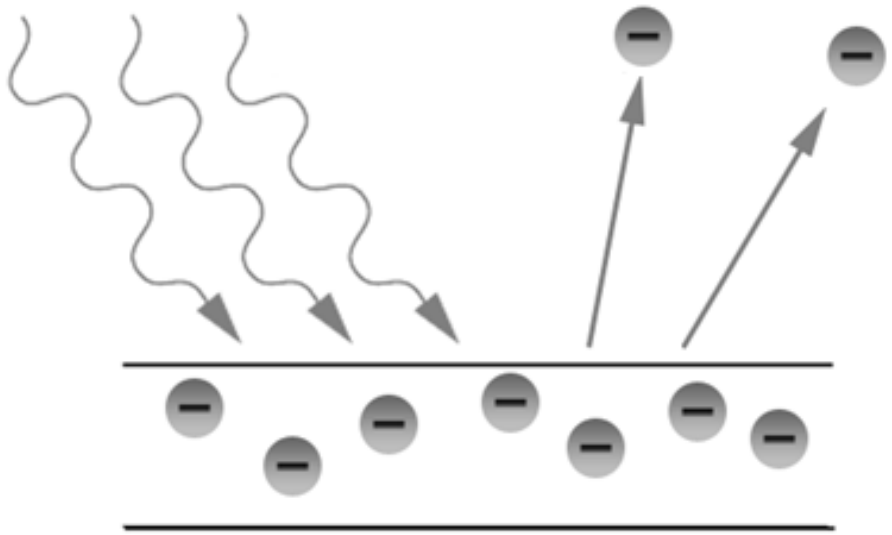

Figure 34. Schematic of the photoelectric effect.

At the present time, photodiodes are the detector of choice for many applications. They convert light into a current due to the photoelectric effect and a special inner structure made of different semiconductor materials. Also our prototype device uses photodiodes as light detectors, because of the wide variety of photodiodes for different wavelengths, low price and high availability.

Important parameters when selecting a photodiode are spectral responsivity, dark current, response time and noise-equivalent power (NEP). Depending on the application at hand, some of these parameters will prevail over the others. In a communication system, for example, response time is an essential parameter, since it limits the maximum usable bandwidth of the system. In our case, one key determinant is spectral responsivity, which is the ratio of generated current to

incident light, expressed in amperes per watt (A/W). An example of spectral responsivity is shown in Figure 37. The other central parameter is NEP, which defines the minimum detectable signal level. Bandwidth, on the other hand, is not important, as the amount of data transmitted in our application is low.

Selection of photodiode is a key point when designing a light detector, because the spectral response of a photodiode is not constant with wavelength. Thus, choosing between different photodiodes depends mainly on the spectral content of the signal to be detected, but also on the noise characteristics of the photodiode. Metal-shielded photodiodes are less susceptible to external noise sources, which is an important consideration, when the signals to detect are comparable to the noise level.

Although the photodiode is an indispensable element for converting light into current, additional circuitry is necessary to convert this current into a voltage level that other devices can work with. For this reason, photodiodes are always part of a circuit known as preamplifier or frontend, which is used to convert the low current generated by the photodiode in a usable voltage level. One commonly used frontend is the transimpedance amplifier, since it reduces the amount of noise sources. [29, 30]

5.2. Physical implementation of detectors

Two basic frontend designs were constructed; the first being the one already used in the old detectors constructed by our research team, due its well-known behavior. A schematic of this frontend is shown in Figure 35.

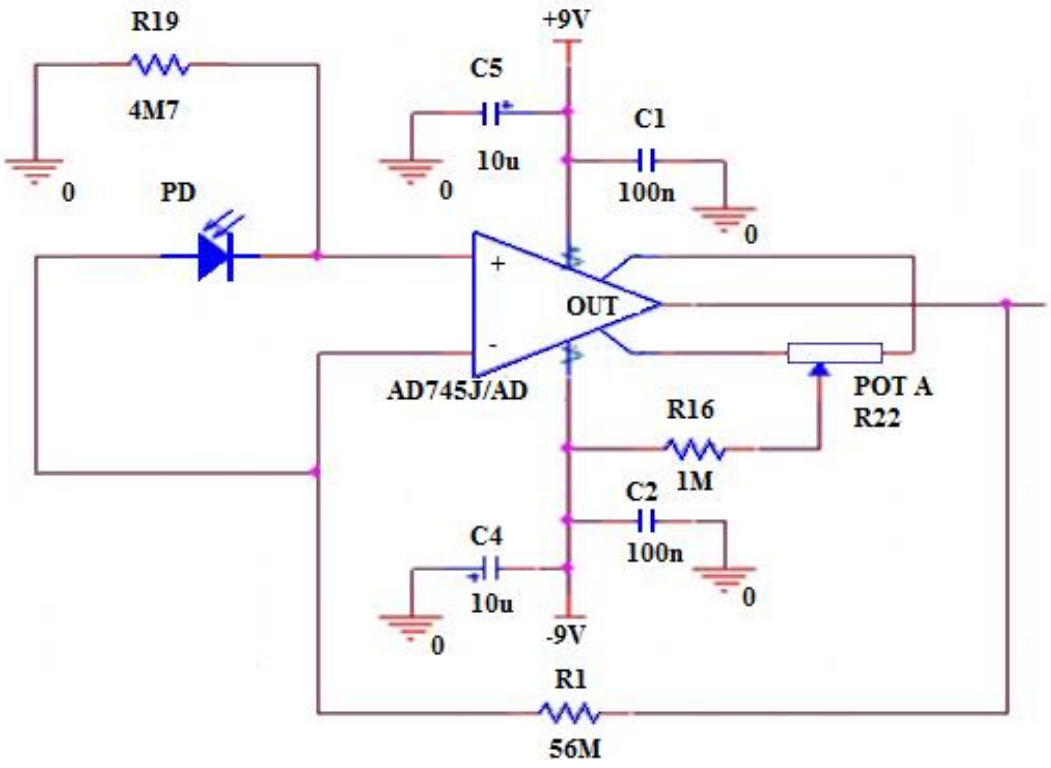

Figure 35. Schematic of the frontend used in the light detectors of the prototype.

This circuit is a simple transimpedance amplifier, whose input voltage is the voltage difference that the photodiode current creates between the pins of the amplifier, the circuit gain is controlled by the feedback resistor R_1. High values of R_1 increase amplification, but also reduce both thermal noise and voltage noise produced by the amplifier, which are the dominant sources of noise. The next equation describes the dependence of thermal and voltage noise on R_f.

$$I_f = \left(\frac{4KTB}{R_f}\right)^{\frac{1}{2}}, \tag{25}$$

$$I_{n\,e} = e_n \cdot \frac{R_{sh}+R_f}{R_{sh}\cdot R_f}, \tag{26}$$

where R_f is the feedback resistor; K=1.381 × 10^{23} J K^{-1} is the Boltzmann constant; B is the bandwidth; T is the temperature; e_n is the amplifier voltage noise and R_{sh} is the shunt resistor. [11]

Capacitors are used for additional filtering of the amplifier's power supply, while POT A is used to control the offset of the circuit. The circuit uses the ultra-low-noise amplifier AD745 and high-responsivity photodiodes.

Four of these detectors were constructed as part of this thesis, two of them made with the high-quality photodiode S2386-18K by Hamamatsu and the other two with the cheap plastic SFH203-P photodiode by OSRAM. Both photodiodes have a responsivity peak in the NIR region. A photograph and a spectral response of them are shown in Figures 36 and 37.

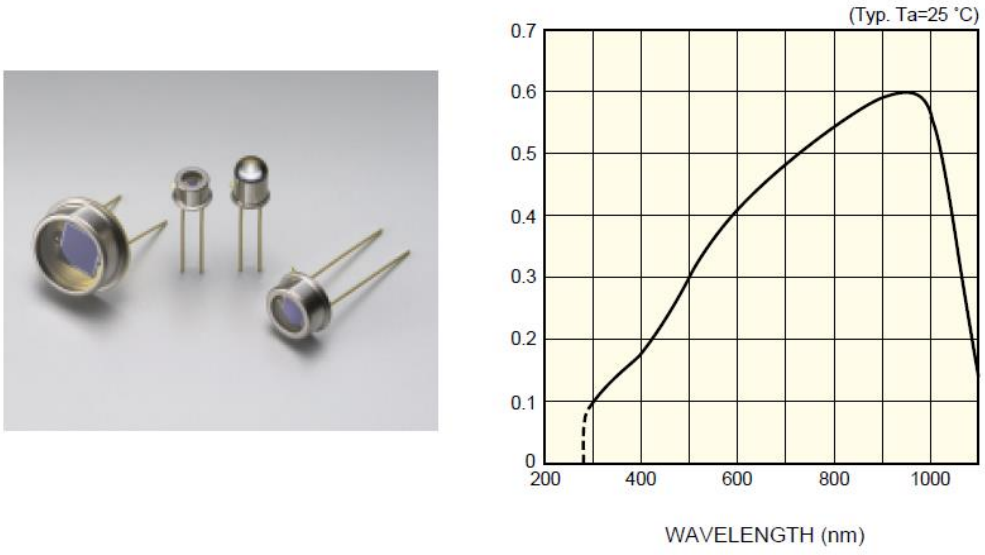

Figure 36. S2386 family of photodiodes from Hamamatsu, on the left, and their spectral response, on the right, adapted from the datasheet for the Si photodiode S2386 series. Values are expressed in A/W, indicating a maximum responsivity of 0.6 A/W at 960nm.

This photodiode was selected, because of its high responsivity in the 800-1000 nm range, which leads to better detection of the NIR signals used in the prototype. The wavelenghts used in the NIR range were 830 nm and 915 nm, allowing deeper penetration in the head. However, attenuation is also higher, necessitating the use of metal-shielded photodiodes to reduce external noise as far as possible. The selected photodiode has an effective area of 1.2 mm^2, which is similar to the transversal area of the optic fiber used to collect light.

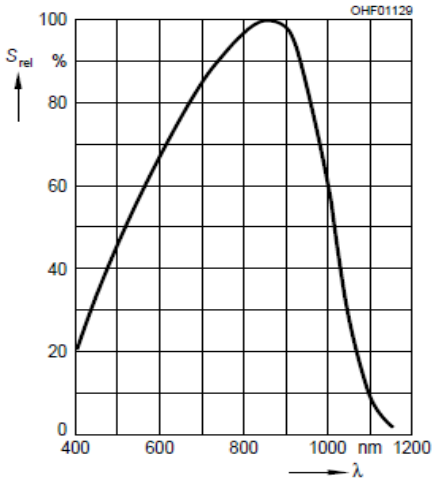

Figure 37. SFH203P photodiode from OSRAM on the left and the relative spectral response on the right, adapted from the datasheets SFH203P and SFH203PFA. Maximum responsivity is 0.62 at 860nm.

This photodiode was selected, because of its low price and high responsivity. Although unshielded, it is more than sufficient for detecting signals from the upper layers of the head from a short distance, since the power of the light is still greater than the noise. An ideal distance range for measurements is between 2 and 3 cm.

The detectors were mounted on small PCBs, which were later placed in the prototype case. Additional circuitry was added to the PCBs, including the same voltage regulators as in the filters to stabilize the power supply. As this design process has already been explained, it will not be repeated here. Also added to the detectors was a second stage of amplification and filtering, offering an option for future implementation. The amplifier is a standard inverting amplifier with room for passive filters in the input and for four different feedback resistors that can be selected with a switch, giving the option of having four different fixed values of amplification. Figure 38 shows a schematic of the second stage of detectors.

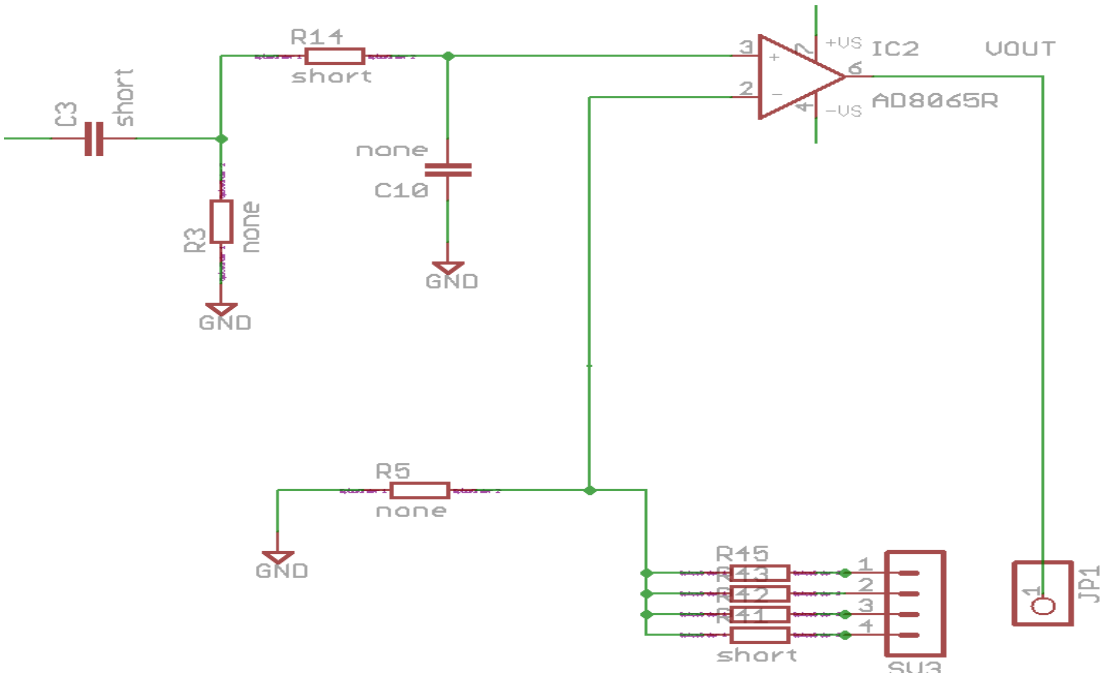

Figure 38. Schematic of the second stage of detectors.

In the final detector setup, the second stages only had one feedback resistor with no gain and, thus, requiring no additional filtering, leaving the footprints of the remaining components available for potential later use.

All the detectors had a supply voltage of 12V, and they were connected to the inner power supply of the prototype with flat wires. The output signal of each detector was connected to one of the inputs of the set of filters designed before. All the PCBs were made with Eagle software. Figures 39 and 40 show the PCB layer of the detectors.

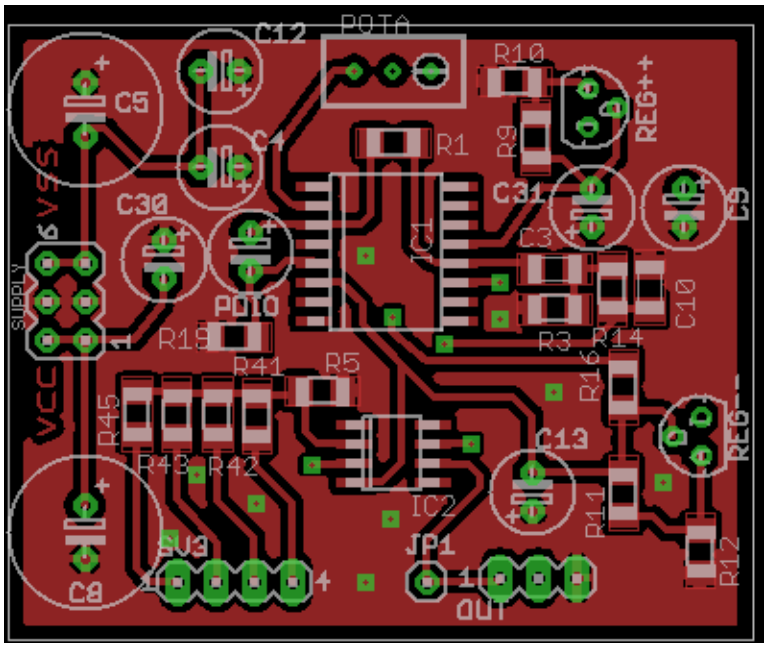

Figure 39. Top layer of the light detector.

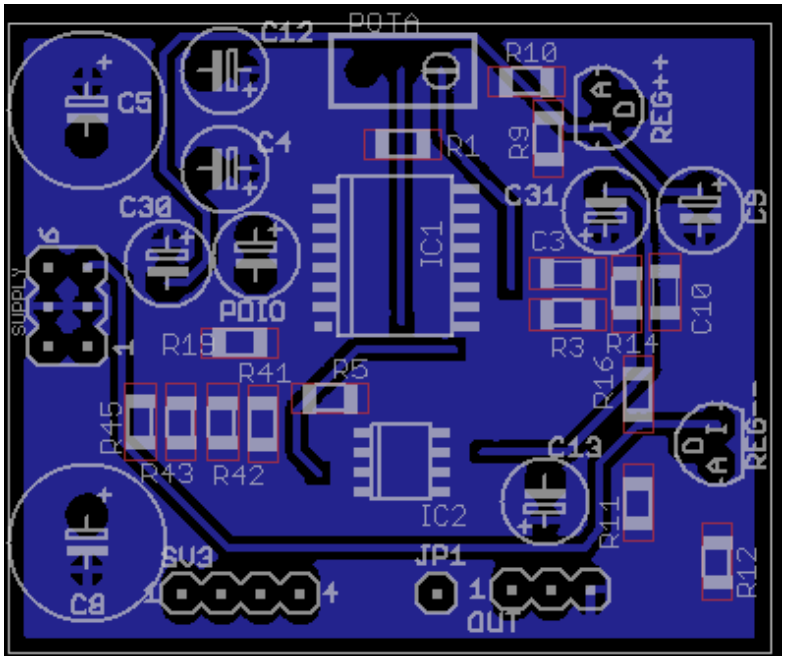

Figure 40. Bottom layer of the light detector.

Once the design of the PCB layout was complete, it was sent to the workshop of the University of Oulu to be fabricated. Soldering of components was done in one of the soldering rooms of the university. Figures 41 and 42 show the detectors.

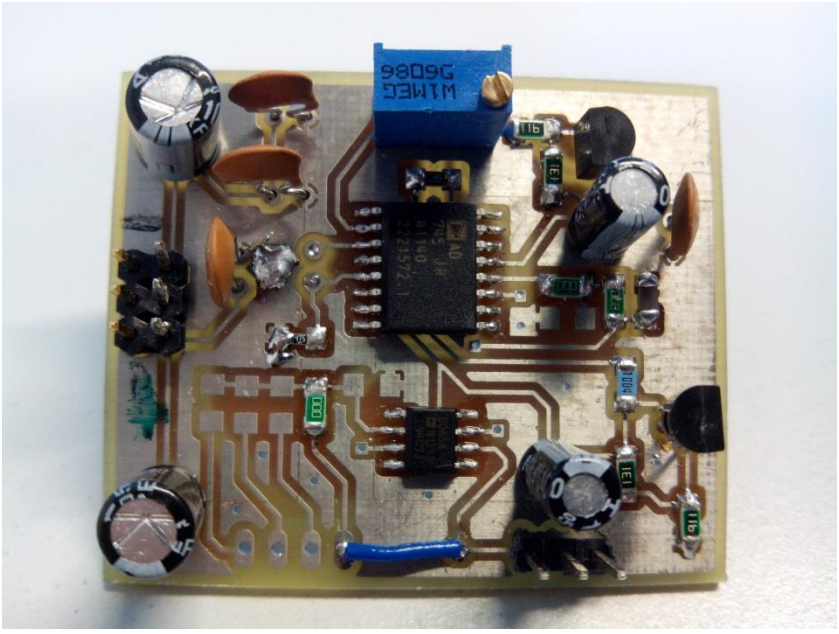

Figure 41. Top view of a light detector.

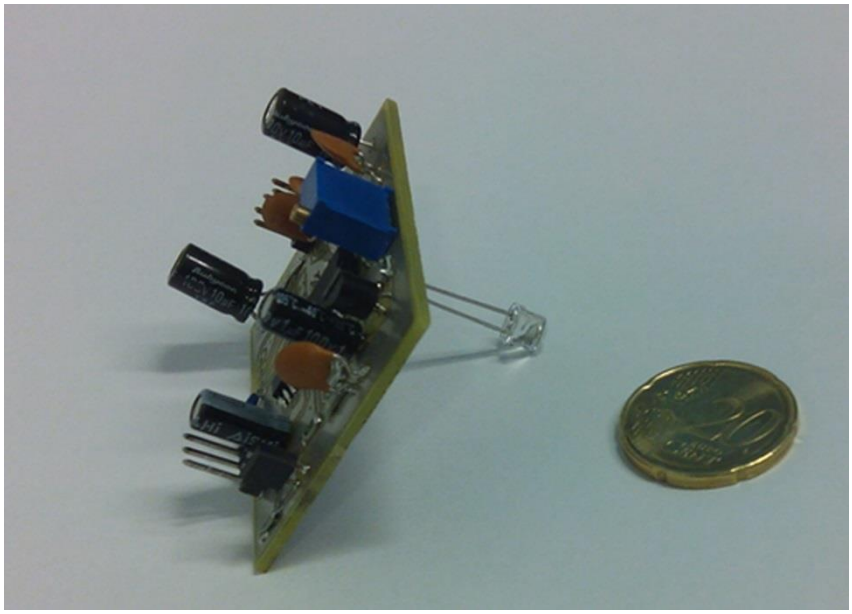

Figure 42. Side view of a light detector.

The design for the other two detectors came from a catalogue of application circuit examples for silicium photodiodes, published by Hamamatsu Photonics. A schematic of the circuit, described as a low-level light sensor frontend, is shown in Figure 43.

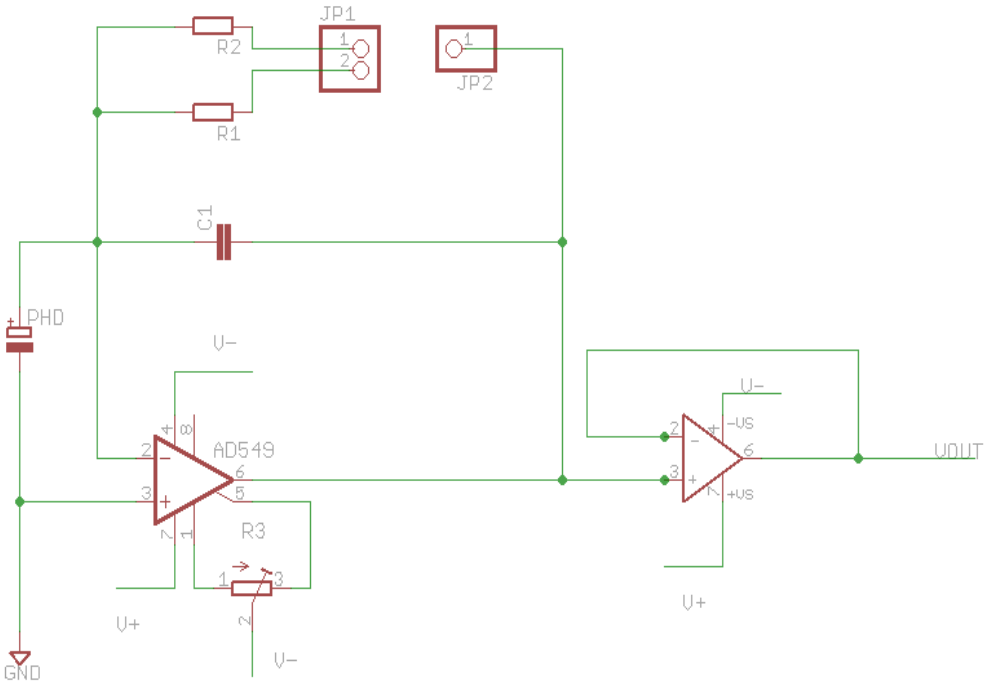

Figure 43. Schematic of Hamamatsu's light detector.

This circuit is very similar to the previous one; gain is controlled by the switchable feedback resistors R1 and R2 and offset voltage by the resistor R3. There is a feedback capacitor for low-pass filtering of signals and the circuit has a second stage in follower configuration, isolating the frontend from the next stages.

What is different in this design is the amplifier. The AD549 is a metal-shielded amplifier with a very low noise level that, in combination with the metal-shielded photodiode S2386-18K from Hamamatsu, was supposed to achieve a very low noise level and great sensitivity. This, in turn, would allow better detection of deeper reflected light.

A cheap amplifier, OP07 from Analog Devices, was selected for the follower stage, because once the frontend has amplified the detected signal, it is no longer susceptible to the low level noise a cheap amplifier might add.

Two of these detectors were implemented on PCBs of the same size as the previous ones and the same voltage regulators were added to the PCBs. Figures 44 and 45 show the PCB layouts.

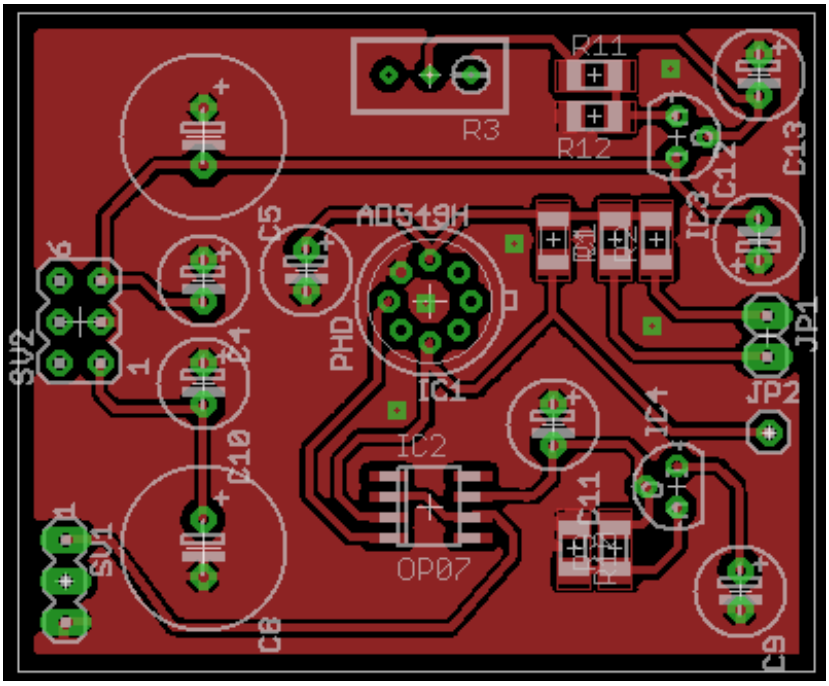

Figure 44. Top layer of the Hamamatsu light detector.

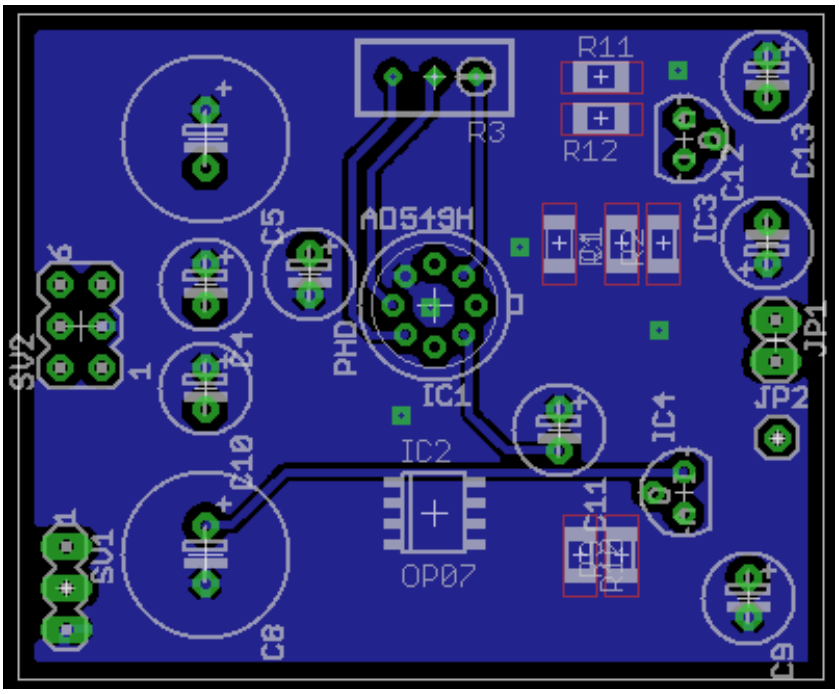

Figure 45. Top layer of the Hamamatsu light detector.

Figures 46 and 47 illustrate the corresponding final PCBs.

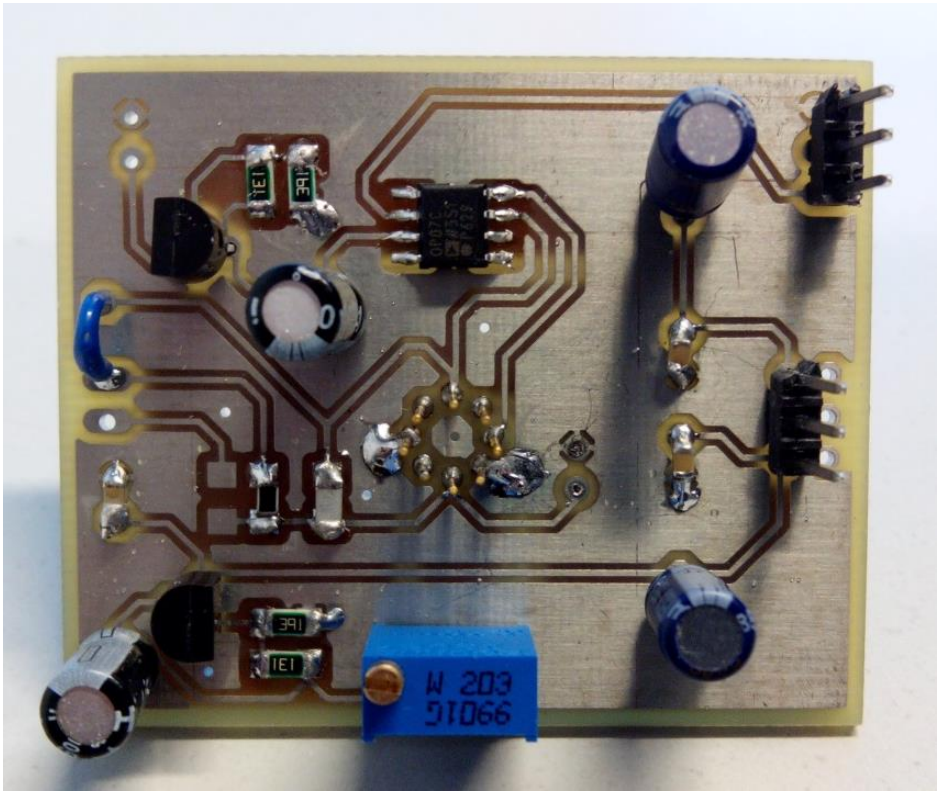

Figure 46. Top view of the Hamamatsu light detector.

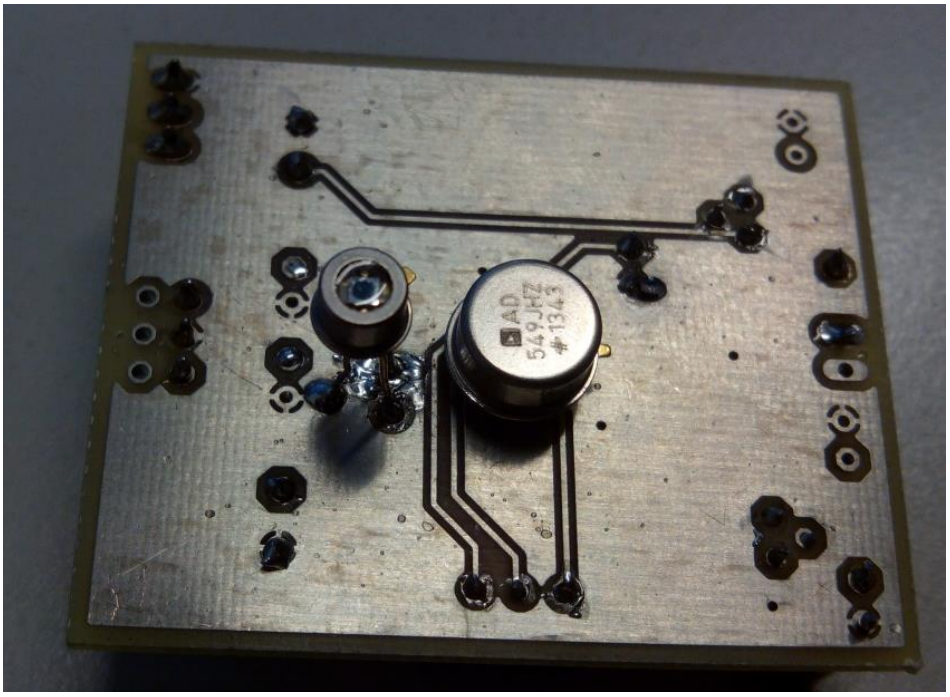

Figure 47. Bottom view of the Hamamatsu light detector, showing the metal-shielded photodiode and amplifier.

5.2.1. Practical Results.

Testing began once the PCBs were fabricated. Light detector testing proved a hard process, because obtaining relevant results for our application demanded using the whole hardware-based system, including the filters designed as part of this thesis and the hardware lock-in amplifiers constructed by the research group. The problem was that the lock-in amplifiers were a first version that had to be tested as well, and when the system failed, the entire chain of circuits had to be checked to determine the error source. In addition, the results could not be compared with those of the fNIRs prototype, because the signals needed processing before any relevant information could be extracted. What is worse is that this hardware analysis was not possible without dismounting the fNIRs prototype - which was being constantly used in medical studies with real patients. For these reasons, it was decided that in testing the light detectors together with the filters and lock-in amplifiers, the signal to be detected would be the pulse measured from the skin, instead of brain signals, because pulse identification requires no additional processing. Heartbeat detection suffices to demonstrate that, after additional work, the system will be able to detect brain signals.

The test setup consisted of two different light sources, one at 830 nm and the other at 660 nm, and some medical probing fibers with a diameter of 1.25 mm. These fibers were needed to guide light to the skin, to collect reflected light and to carry it to the detectors, which were connected in a chain with the filters and they, in turn, with the lock-in amplifiers. An oscilloscope was used to observe the output of the lock-in amplifier at the same time as the patient's heart rate was measured by a non-

invasive near-infrared photoplethysmogram (PPG) meter, property of the laboratory. The PPG meter provides a corresponding heart rate reading, allowing comparison of results.

The first step in testing involved detecting the modulating signal emitted by the light source through the finger and on the forehead. The distance between the light source and the receiver fibers was 3 cm.

Detectors based on the old version were tested with filters, the measured signals being the output of the detector and filter outputs. Figure 50 shows light detected on the forehead first without filters and then with filters, while Figure 32 shows the same signal detected from the finger before and after filtering.

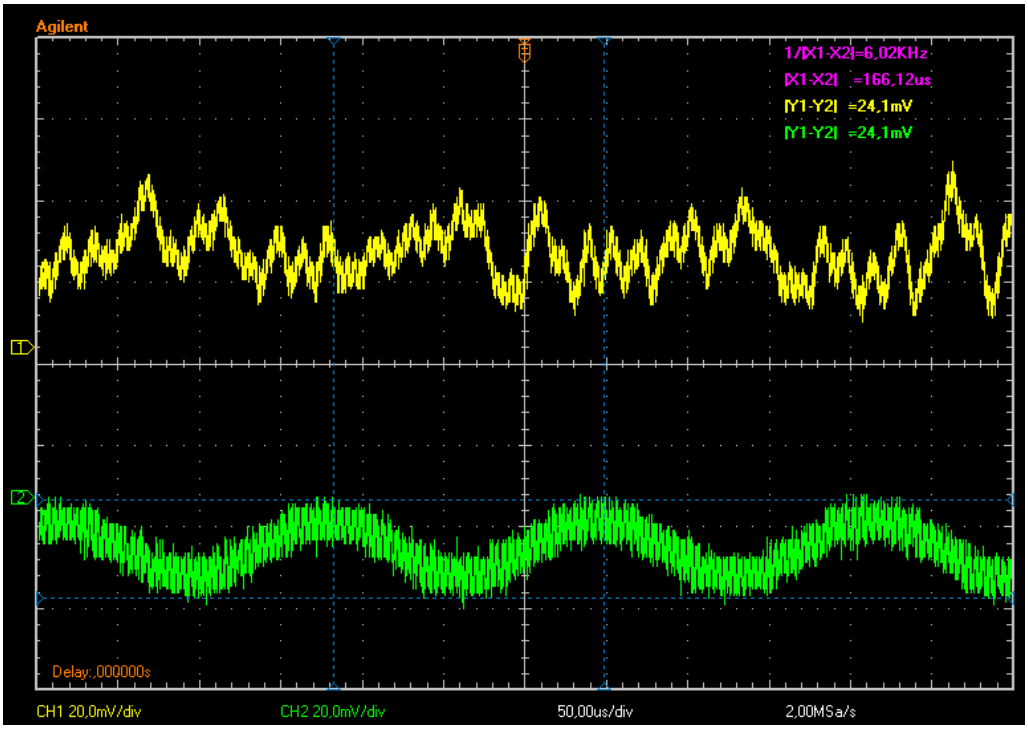

Figure 48. Detected signal on the forehead, signal 1, and filtered signal, number 2.

The second part of testing was conducted by connecting the lock-in amplifiers to detect pulses from the forehead skin. Figure 49 compares pulses detected through the finger by the PPG meter and our system.

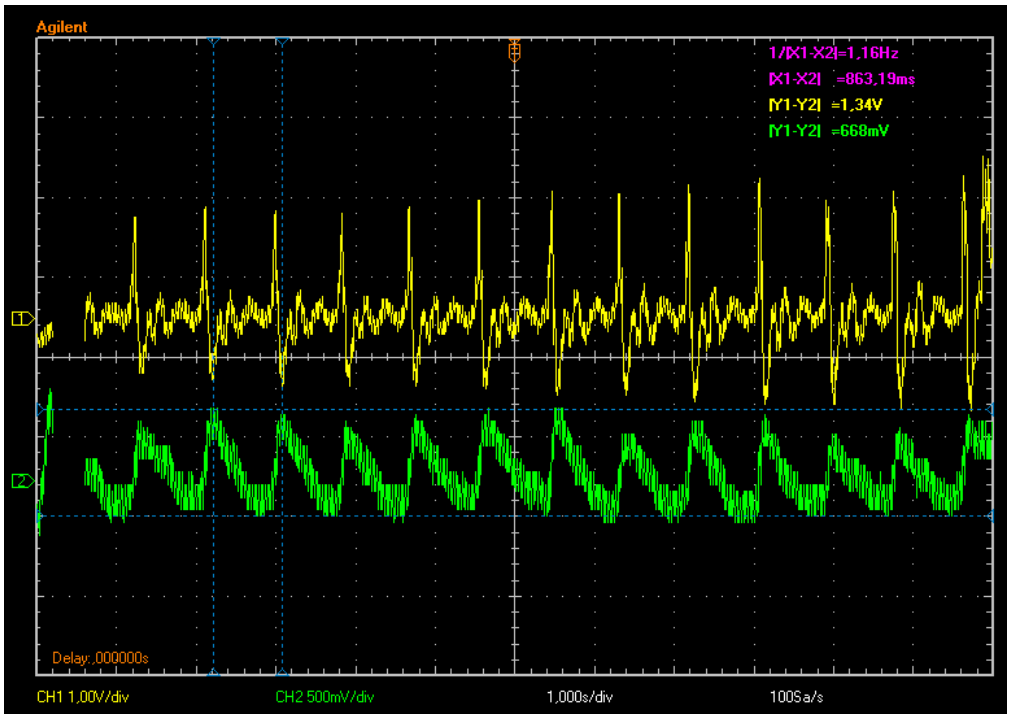

Figure 49. Pulse detected with the PPG from a finger, signal number 1, vs pulse detected with the detectors+filters+lock-in amplifiers on the forehead using a source-detector distance of 3 cm.

Also the new detector version was tested, but we realized during testing that the design had some serious problems when used for this application. Chief among these was the fact that the configuration requires high amplification, because the feedback resistor has to be very high, of the order of 1GΩ. In addition, with the feedback capacitor in place, very low frequencies were filtered out, as shown in this equation:

$$fc = \frac{1}{2\pi R_f C_f} = \frac{1}{2\pi \cdot 1.10^{9}\Omega \cdot 1.10^{-12}\, F} = 159.15\, Hz\ , \qquad (26)$$

where f_c is the cutoff frequency, R_f is the feedback resistor and C_f is the feedback capacitor.

As a result, the signals to be detected, 6, 7, 8 and 9 KHz, were completely removed and could not be detected. Since the capacitor was the lowest available in the laboratory and lowering Rf was not an option, we decided to change the design by modifying the PCB. To that end, the feedback capacitor was removed and gain was divided between the two stages of the circuit. In addition, the feedback resistor of the first stage was lowered to 82 MΩ, and the second stage was changed from a simple follower to an inverting amplifier by the addition of two resistors. This combination of two stages served to increase gain by a factor of 14. Finally, a simple passive high-pass filter was added between the two stages to remove the 50 Hz noise coming from the power supply.

After these modifications, we tried detecting modulation signals from the forehead. Figure 50 shows the detected signal before and after filtering, at the light modulation frequency of 6 kHz.

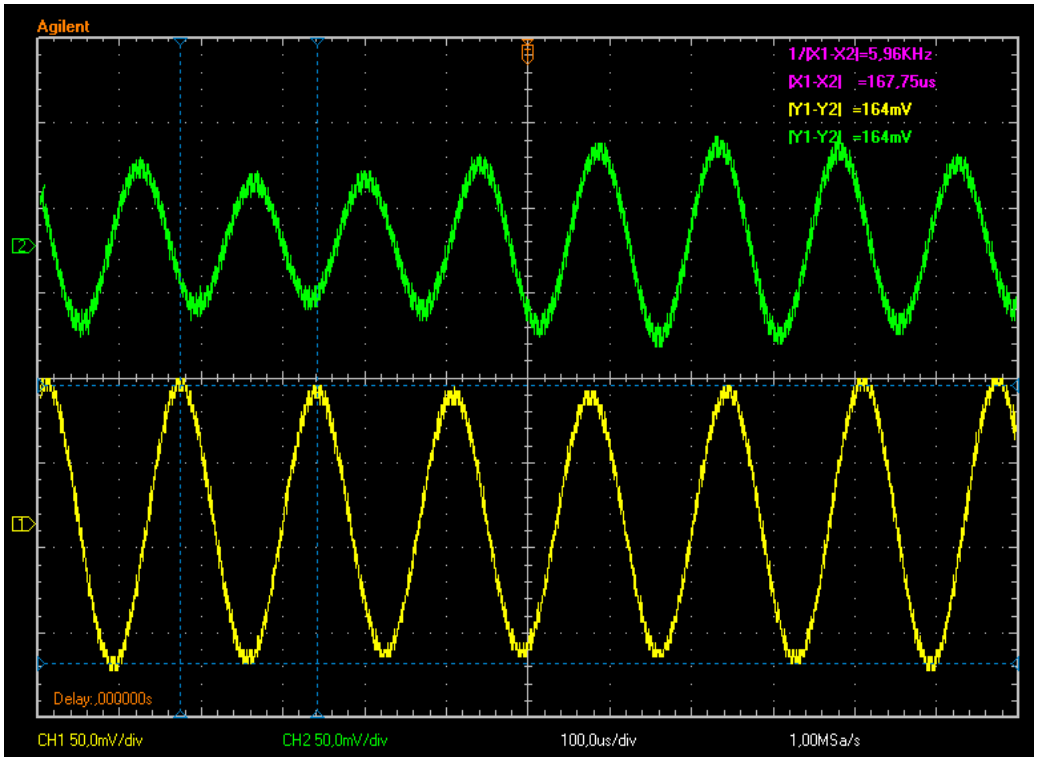

Figure 50. Detected signal, number 1, and filtered signal, number 2.

As seen in Figure 50, the signal level is very low, around 160mV, because the measuring distance was 3 cm. After filtering, the lock-in amplifiers extract the envelope of the signal, which holds hemodynamic information.

Unfortunately, further testing of detectors was not possible, because the prototype was being actively used at the time. Even so, the obtained results clearly indicate successful light detection. Simultaneously with circuit testing, a new, lighter and smaller metallic case for the prototype was being constructed in the workshop. On completion, the light detectors and filters were mounted on the new case. Shown in Figure 51 is a circuit mounted on the new metallic case of the prototype.

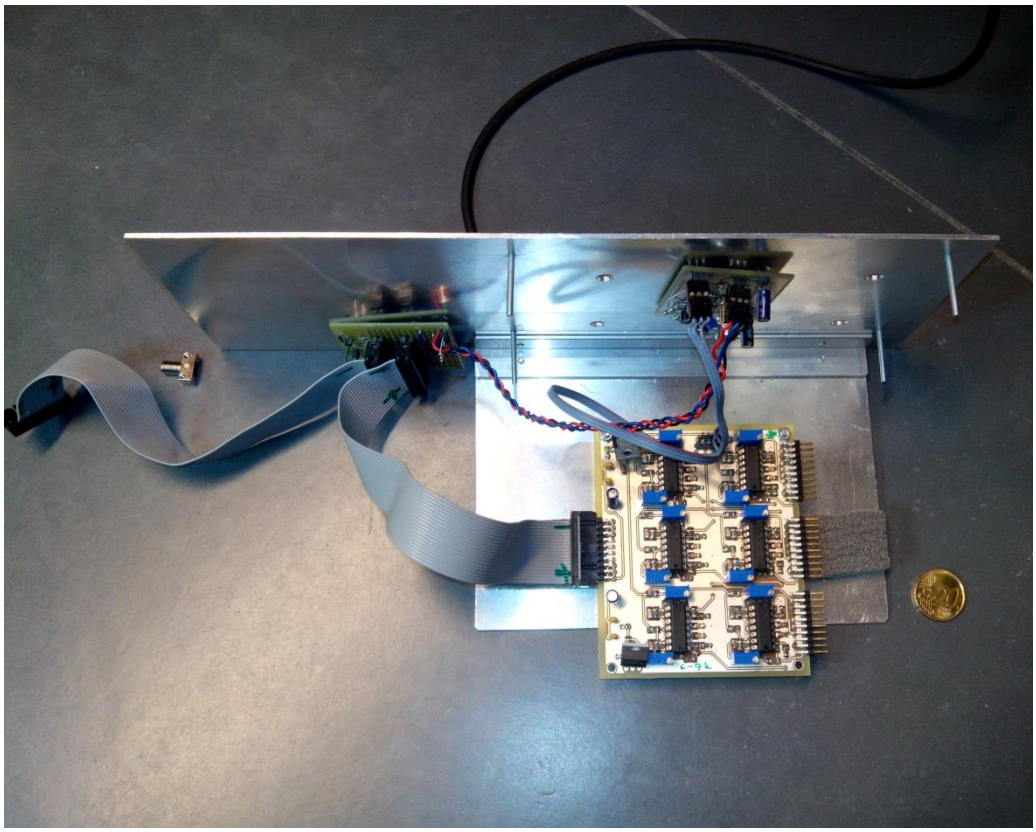

Figure 51. Detector + filters mounted on the metallic case of the prototype.

Although the photo only shows one circuit, the holes indicate where the other circuits are to be mounted. All filter PCBs and lock-in amplifiers will be stacked on top of each other in the same position. Also visible in the photo is the optic fiber used to guide light. When finished, the prototype will house a total of 6 fibers, each connected to a detector.

6. DISCUSSION

This master's thesis forms part of a bigger project and the work was driven by the deadlines and busy schedule of the research group during the eight month period which the research leading up to this thesis was conducted. It was a great challenge, due to the different topics I had to learn about, including fNIRs technology, filter design, amplifier design, light detector design, voltage regulator design, ORCAD simulations, PCB design in EAGLE, soldering of electronic components and, of course, testing of electronic circuits.

Fortunately, all project objectives were finally achieved; every circuit designed proved fully functional and now awaits further testing. This will happen when the research group gets to put the hardware version of the prototype to real tests.

Four sets of filters were designed; one set was for 1, 2, 3 and 4 kHz, which served to test the configuration and its characteristics. Testing how the circuits respond to component changes provided useful information, which was used in designing the final filters. This circuit taught us how to tune the central frequency of the filters, how to control gain, how to modify the passing band and what the limits for the relevant values are. After hard testing, which included soldering and unsoldering of components, the PCB was too damaged to use. The second set of filters was the final version for 1, 2, 3 and 4 kHz. With this PCB, filters were tested in combination with lock-in amplifiers, to enhance performance. Different ways of connecting the PCBs were considered, and after tests it was decided to use flat wires. These filters can be shifted up to 7 kHz without significant changes in behaviour, thanks to the potentiometers included in the design. After this test period, it was decided to keep using the same frequencies as in the prototype, i.e., 6, 7, 8 and 9 kHz.

The final version of the filters was designed for 6, 7, 8 and 9 kHz. Thanks to the lessons learned from the previous versions and the hard testing conducted on other boards, the design and manufacture of these filters was a quick and clean process with very good results. Two PCBs were constructed, with 12 filters each. All filters were tested separately to ensure correct performance. They were then used in testing the detectors and lock-in amplifiers. After tuning, they were ready to be included in the hardware version of the fNIRs device.

The implemented filters were very good approximations of their theoretically calculated counterparts, with very similar transfer functions in areas of interest. Moreover, their behaviour was stable and they could be fine-tuned with the included potentiometers. As the relevant figures show, their characteristics were confirmed by our tests. Most importantly, they have the ability to filter a periodic signal that is under the level of noise, to reconstruct it and to remove a major part of unwanted noise, see Figure 48. In conclusion, it can be said that filter design was a success and that the goals set for the filters were achieved.

The second part of this work included the design of six light detectors. Four of these were made using the same configuration as the detectors used in the fNIRs prototype, while the other two were made using a schematic provided by the manufacturer, Hamamatsu Photonics.

The four detectors based on the old version comprised the ultra-low noise amplifier AD745. Two of these used the S2386-18K photodiode in a metal case and the other two the plastic photodiode SFH203P. Both designs were tested and proved capable of properly detecting light signals, although a comparison of results could not be performed due to lack of resources and time. Both circuits were able to detect

light through the finger and on the forehead, which is a relevant result for the intended application.

The other detectors were made following a schematic from the manufacturer, Hamamatsu. The detectors were coupled to the metal-shielded ultra-low noise amplifier AD549 from Analog Devices and the metal-shielded S2386-18K photodiode from Hamamatsu.

After implementation, the detectors underwent testing, in which a problem emerged. It turned out that the feedback loop was filtering signals above 160 Hz, due to the high feedback resistor used. To eliminate that effect, the circuit was modified. Modification involved removing the capacitor in the feedback loop and dividing the gain of the circuit into two parts, lowering the feedback resistor from 1GΩ to 82MΩ and, lastly, converting the follower stage into an inverting amplifier by adding two resistors.

With these changes, the detectors started functioning properly at the frequencies we were using, and additional testing demonstrated detection of light through a finger and through forehead skin. As said before, comparison between the different circuits was impossible in part due to lack of time and resources and in part due to the need of a fully functional hardware prototype. Despite this, the results can be considered good and the detectors will be used by the research group to test, develop and improve the fNIRs system.

Finally, testing of both circuits was conducted with the lock-in amplifiers designed by the group. These tests were successful, and the chain of circuits working together was able to detect pulses through a finger and on the forehead.

To summarize, the research group found the work described in this thesis helpful and it will assist their future efforts to develop and investigate the fNIRs system and its applications.

7. FUTURE RESEARCH

Medical application of NIR technology still has a long way to go, and there are multiple approaches and options that require investigation and development. One direction of research focuses on improving the hardware technology of NIR devices. This includes improving the sensitivity and lowering the cost of this technology, downsizing equipment, and so on. The ultimate goal in hardware improvement is a wearable fNIRs system, which in combination with wireless technologies will allow continuous brain health monitoring at home. [31]

Other highly useful applications of this technology await exploration. For example, NIR technology can be useful in the detection and elimination of different kinds of tumours and cancers. Detection of skin melanomas is still a process that relies on the expert eye of a well-trained physician. NIR technology can be used to automatically detect melanomas by comparing the absorption spectra of tumour cells with those of normal cells [30]. Also breast cancer lends itself to NIR-based detection based on abnormal hemoglobin concentration and oxygen saturation [32]. Other lines of investigation focus on using different substances that only stick to tumour cells that are sensitive to NIR light. This helps to improve the contrast of the tumour region or even to heat tumour tissue until it is destroyed by the same NIR light [33].

Perhaps the most promising goal for fNIRs technology itself is the emergence of multimodal systems that allow a better understanding of both fNIRS results and cerebrovascular responses to neuronal stimuli. Methods involving blood dyes are being performed in combination with fNIRs systems to allow measuring cerebral blood volume (CBV) and cerebral blood flow (CBF). [10, 11, 34]

7.1. Multimodal systems

Mapping of the human brain is a complex undertaking that cannot be achieved by a single measurement. In fact, multiple parameters and correlations between them must be recorded in order to get a better understanding of cortical activity and neurovascular coupling. For this reason, multimodal systems are being designed in many places. One such multimodal setup has been developed in Oulu, Finland, in close cooperation between the Optoelectronics and Measurement Techniques Laboratory of the University of Oulu and the Oulu Functional Neuroimaging (OFNI) group based at the Oulu University Hospital. At the present time, the setup consists of seven independent measurement and imaging modalities that can be used simultaneously and in synchrony. Significantly, this setup includes EEG, fMRI and NIBP in combination with fNIRS systems. [35, 36]

Combining EEG with fNIRs enables recording electrical and hemodynamic changes and offers a promising tool for the study of language-related cerebral activity. It is also applicable to the evaluation of epileptic patients and to their daily clinical routine management. EEG provides very high temporal resolution, which can be complemented by the higher spatial resolution of fNIRS. Thus, combined data can provide neurophysiological data of the cortex area with high temporal and spatial resolution [19, 37].

fMRI is the diagnostic method of choice for recording normal, pathological or injured brain processes *in vivo*, as well as for assessing potential risks of surgery or

other invasive treatments of the brain. fMRI systems measure blood oxygenation level-dependent signals (BOLD) to extrapolate related brain cell activity from these signals. However, as this relation remains unclear, fNIRS offers a powerful tool to resolve these questions, since it allows measuring total changes in HbO2 and Hb, which are strongly correlated with BOLD signals. [19, 38]

Combined fMRI-fNIRS systems can be used to elucidate BOLD response biophysics. While fNIRS has a better temporal resolution (40 ms instead of 2000 ms) fMRI offers superior spatial resolution and whole-head coverage for BOLD changes. Further optimization of the combined method may allow quantification of different blood flow parameters, such as oxygen extraction fraction or CBV. [19, 38]

Using fMRI in combination with an fNIRS system requires special construction measures for the NIRS system. No ferromagnetic materials can be used in the NIRS device, because they may affect the strong magnetic fields generated by the MRI scanner. However, small amounts of ferromagnetic material can be used, provided that components containing these materials are placed outside the magnetic field. In addition, electromagnetically-sealed structures must be used to avoid mutual electromagnetic influence. [11]

8. CONCLUSION

This thesis set out to improve specific components used in the light-detection hardware that forms the core of a frequency-domain/spatially-resolved fNIRS system. All work toward that end was carried out in the Optoelectronics and Measurement Techniques Laboratory of the University of Oulu and has served to facilitate the further development of the fNIRS prototype constructed there.

Different narrow bandpass filter configurations were analyzed and compared to select the best option for the system. After evaluation of all alternatives, multifeedback filters and resonator filters were designed and simulated. Finally, two different sets of resonator filters were physically implemented with printed circuit technology.

The second part of the thesis involved manufacturing six low-noise, high-sensitivity NIR light detectors to extend the system's light detection capabilities. These detectors were implemented on printed circuit boards. After implementation, the circuits were tested separately and in combination with other parts of the system, achieving good results in both cases. The filters were tested for different input characteristics of the input signal, giving excellent results in signal filtering, even recovering signals below the level of noise. Once the detectors were tested and found problems solved, they proved capable of detecting light from the forehead and finger. The most significant result was the detection of blood flow pulsations from the finger and forehead of a subject using both detector and filter circuits in combination with lock-in amplifiers and the same principles and testing setup as with the fNIRS device.

9. REFERENCES

[1] Nilsson R. Applications of Near Infrared Spectroscopic Analysis in the Food Industry and Research, Food Safety Centre, Tasmanian Institute of Agricultural Research, University of Tasmania, Australia.

[2] Burns DA, Ciurczak EW. (2007). Handbook of Near-Infrared Analysis, Third Edition. CRC Press, London, 826 p.

[3] Bozkurt A, Rosen A, Rosen H, Onaral B. (2005). A portable near infrared spectroscopy system for bedside monitoring of newborn brain. BioMedical Engineering OnLine, 4:29 doi: 10.1186/1475-925X-4-29. http://www.biomedical-engineering-online.com/content/4/1/29

[4] Izzetoglu K, Ayaz H, Merzagora A, Izzetoglu M, Shewokis PA, Bunce SC, Pourrezaei K, Rosen A and Onaral B. (2011). The evolution of field deployable fnir spectroscopy from bench to clinical settings. J. Innov. Opt. Health Sci. 04, 239, DOI: 10.1142/S1793545811001587

[5] Henderson R. (2007). Wavelength considerations. Instituts für Umform- und Hochleistungs. Retrieved on 2007-10-18.

[6] Lubbock C. (1933). The Herschel Chronicles, vol.1, William Herschel museum, Bath, UK. Originally published in 1933 by Cambridge University Press.

[7] Jobsis F. (1977). "Noninvasive, infrared monitoring of cerebral and myocardial oxygen sufficiency and circulatory parameters". Science 198 (4323): 1264–1267. doi:10.1126/science.929199

[8] Ferrari M, Giannini I, Sideri G, Zanette E. (1985). Continuous non invasive monitoring of human brain by near infrared spectroscopy. Advances in experimental medicine and biology 191: 873–882. doi:10.1007/978-1-4684-3291-6_88

[9] Il-Young S, Birsen Y. (2006). Advances in Sensing with Security Applications. pp 341-372. DOI:10.1007/1-4020-4295-7_15

[10] Näsi T. (2013). Multimodal applications of functional near-infrared spectroscopy. Aalto University.

[11] Sorvoja HSS, Myllylä TS, Kirillin MYu, Sergeeva EA, Myllylä RA, Elseoud AA, Nikkinen J, Tervonen O, Kiviniemi V. (2012). Non-invasive, MRI-compatible fibreoptic device for functional near-IR reflectometry of human brain. Quantum Electronics (Impact Factor: 0.82); 40(12):1067. DOI: 10.1070/QE2010v040n12ABEH014503

[12] Prahl S. (1999). Optical Absorption of Hemoglobin. Oregon Medical Laser Center. http://omlc.org/spectra/hemoglobin/index.html (Accessed 11.10.2014)

[13] Jue T, Masuda K. (2013). Application of Near Infrared Spectroscopy in Biomedicine. Springer; 2013 edition (March 21, 2013). 151 p.

[14] Adapted from http://commons.wikimedia.org/wiki/File:HbAbs_v3.png (Accessed 11.10.2014)

[15] Tuchin VV. (2007). Tissue Optics: Light Scattering Methods and Instruments for Medical Diagnosis. Bellingham, SPIE Press. DOI: 10.1117/3.684093.

[16] Korhonen VO, Myllyla TS, Kirillin MY, Popov AP, Bykov AV, Gorshkov AV, Sergeeva EA, Kinnunen M, Kiviniemi V. (2014). Light Propagation in NIR Spectroscopy of the Human Brain, Selected Topics in Quantum Electronics, IEEE Journal of (vol.20, Issue:2, pp.1,10) March-April 2014, doi: 10.1109/JSTQE.2013.2279313

[17] Wyatt JS, Cope M, Delpy DT, Richardson CE, Edwards AD, Wray S & Reynolds EO. (1990). Quantitation of cerebral blood volume in human infants by near infrared spectroscopy. J Appl Physiol 68(3): 1086–1091

[18] Cope M. (1991). The application of near infrared spectroscopy to non-invasive monitoring of cerebral oxygenation in the newborn infant. Department of Medical Physics and Bioengineering: 342.

[19] Bakker A, Smith B, Ainslie P and Smith K. (2012). Near-Infrared Spectroscopy, Applied Aspects of Ultrasonography in Humans, Prof. Philip Ainslie (Ed.), ISBN: 978-953-51-0522-0, InTech, DOI: 10.5772/32493. Available from: http://www.intechopen.com/books/applied-aspects-of-ultrasonography-in-humans/near-infrared-spectroscopy (Accessed 17.11.2014)

[20] Boas DA, Chen K, Grebert D & Franceschini MA. (2004). Improving the diffuse optical imaging spatial resolution of the cerebral hemodynamic response to brain activation in humans. Opt Lett 29: 1506–1508.

[21] Murkin JM and Arango M. (2009).Near-infrared spectroscopy as an index of brain and tissue oxygenation. Published by Oxford University Press on behalf of the British Journal of Anaesthesia.

[22] Subramaniam K, Park KW, Subramaniam B. (2011). Anesthesia and Perioperative Care for Aortic Surgery. Springer Science & Business Media, 6/1/2011 - 462 pp.

[23] Myllylä T, Korhonen V, Surażyński Ł, Zienkiewicz A, Sorvoja H & Myllylä R (2014) Measurement of cerebral blood flow and metabolism using high power light-emitting diodes. Measurement 58(0): 387-393.

[24] Antoniou A. (1993). Digital Filters: Analysis, Design, and Applications, New York, NY: McGraw-Hill.

[25] Savant C, Roden M, Carpenter G. (1992). Diseño Electrónico Circuitos y sistemas. Adisson-Wesley

[26] Huircán J. (2012). Filtros activos, conceptos básicos y diseño. Universidad de La Frontera.

[27] Narinder K. (2008). Comprehensive Physics XII. Laxmi Publications.

[28] George R. (2003). Detection of Light From the Ultraviolet to the submillimeter, 2nd Edition.

[29] Mohr PJ, Taylor BN, and Newell DB. (2011). The 2010 CODATA Recommended Values of the Fundamental Physical Constants (Web Version 6.0). National Institute of Standards and Technology, Gaithersburg http://physics.nist.gov

[30] Hobbs PCD. (2001). Photodiode Front Ends. The real story. Optics and Photonics News, Vol. 12, Issue 4, pp. 44-47.

[31] Piper S, Kruger A, Koch SP, Mehnert J, Habermehl C, Kang KA, Chang C, and Bruley DF. (2014). A Wearable Multi-channel NIRS Imaging System for Brain Imaging in Freely Moving Subjects. Charité University Medicine Berlin, Department of Neurology

[32] Cao M, Kang KA, Chang C, Bruley DF. (1997). Skin Cancer Detection Based on NIR Image Analysis. University of Maryland Baltimore County.

[33] Cheng X, Mao J, Bush R, Kopans DB, Moore RH and Chorlton M. (2003). Breast cancer detection by mapping hemoglobin concentration and oxygen saturation. Photonify Technologies, Inc.

[34] Kam N. W. S., O'Connell M., Wisdom J. A., and Dai H. (2005) Carbon nanotubes as multifunctional biological transporters and near-infrared agents for selective cancer cell destruction. California Institute of Technology.

[35] Korhonen VO, Hiltunen TK, Myllylä TS, Wang S, Kantola J, Nikkinen J, Zang YF, Levan P, Kiviniemi V. (2014). Synchronous multi-scale neuroimaging environment for critically sampled physiological analysis of brain function- Hepta-scan concept. Brain Connect. 2014 Aug 16. [Epub ahead of print]

[36] Myllylä T. (2014). Multimodal biomedical measurement methods to study brain functions simultaneously with fMRI, doctoral thesis, Acta Univ. Oul. C 497, 2014.

[37] Safra EJ. Brain reseach Center for the study of Learning Disabilities, Faculty of Education, Universitiy of Haifa.

http://ejsafra.haifa.ac.il/index.php/technology/119-fnirs (Accessed 20.10.2014)

[38] Tong Y & Frederick BD. (2010). Time lag dependent multimodal processing of concurrent fMRI and near-infrared spectroscopy (NIRS) data suggests a global circulatory origin for low-frequency oscillation signals in human brain. Neuroimage 53(2): 553–564